# Coherence of Mach fronts during heterogeneous supershear earthquake rupture propagation: Simulations and comparison with observations

A. Bizzarri,[1] Eric M. Dunham,[2,3] and P. Spudich[4]

Received 24 July 2009; revised 18 February 2010; accepted 25 February 2010; published 3 August 2010.

[1] We study how heterogeneous rupture propagation affects the coherence of shear and Rayleigh Mach wavefronts radiated by supershear earthquakes. We address this question using numerical simulations of ruptures on a planar, vertical strike-slip fault embedded in a three-dimensional, homogeneous, linear elastic half-space. Ruptures propagate spontaneously in accordance with a linear slip-weakening friction law through both homogeneous and heterogeneous initial shear stress fields. In the 3-D homogeneous case, rupture fronts are curved owing to interactions with the free surface and the finite fault width; however, this curvature does not greatly diminish the coherence of Mach fronts relative to cases in which the rupture front is constrained to be straight, as studied by Dunham and Bhat (2008a). Introducing heterogeneity in the initial shear stress distribution causes ruptures to propagate at speeds that locally fluctuate above and below the shear wave speed. Calculations of the Fourier amplitude spectra (FAS) of ground velocity time histories corroborate the kinematic results of Bizzarri and Spudich (2008a): (1) The ground motion of a supershear rupture is richer in high frequency with respect to a subshear one. (2) When a Mach pulse is present, its high frequency content overwhelms that arising from stress heterogeneity. Present numerical experiments indicate that a Mach pulse causes approximately an $\omega^{-1.7}$ high frequency falloff in the FAS of ground displacement. Moreover, within the context of the employed representation of heterogeneities and over the range of parameter space that is accessible with current computational resources, our simulations suggest that while heterogeneities reduce peak ground velocity and diminish the coherence of the Mach fronts, ground motion at stations experiencing Mach pulses should be richer in high frequencies compared to stations without Mach pulses. In contrast to the foregoing theoretical results, we find no average elevation of 5%-damped absolute response spectral accelerations (SA) in the period band 0.05–0.4 s observed at stations that presumably experienced Mach pulses during the 1979 Imperial Valley, 1999 Kocaeli, and 2002 Denali Fault earthquakes compared to SA observed at non-Mach pulse stations in the same earthquakes. A 20% amplification of short period SA is seen only at a few of the Imperial Valley stations closest to the fault. This lack of elevated SA suggests that either Mach pulses in real earthquakes are even more incoherent that in our simulations or that Mach pulses are vulnerable to attenuation through nonlinear soil response. In any case, this result might imply that current engineering models of high frequency earthquake ground motions do not need to be modified by more than 20% close to the fault to account for Mach pulses, provided that the existing data are adequately representative of ground motions from supershear earthquakes.

**Citation:** Bizzarri, A., E. M. Dunham, and P. Spudich (2010), Coherence of Mach fronts during heterogeneous supershear earthquake rupture propagation: Simulations and comparison with observations, *J. Geophys. Res.*, *115*, B08301, doi:10.1029/2009JB006819.

[1]Istituto Nazionale di Geofisica e Vulcanologia, Sezione di Bologna, Bologna, Italy.

[2]Department of Earth and Planetary Sciences and School of Engineering and Applied Sciences, Harvard University, Cambridge, Massachusetts, USA.

[3]Now at Geophysics Department, Stanford University, Stanford, California, USA.

[4]U.S. Geological Survey, Menlo Park, California, USA.


0148-0227/10/2009JB006819

## 1. Introduction

[2] In the 1960s it was generally accepted that earthquake ruptures would propagate at the Rayleigh or shear wave speed at maximum. In the last four decades, the problem of ruptures propagating at velocities greater than the *S* wave speed has been the subject of a quite large number of studies, including analytical [*Burridge*, 1973; *Freund*, 1979; *Broberg*, 1994, 1995; *Samudrala et al.*, 2002], numerical [*Andrews*, 1976; *Das and Aki*, 1977; *Das*, 1981; *Day*, 1982; *Okubo*, 1989; *Needleman*, 1999; *Bizzarri et al.*, 2001; *Fukuyama and Olsen*, 2002; *Bernard and Baumont*, 2005; *Bizzarri and Cocco*, 2005; *Dunham et al.*, 2003; *Dunham and Archuleta*, 2005; *Bhat et al.*, 2007; *Dunham*, 2007], and experimental [*Wu et al.*, 1972; *Rosakis et al.*, 1999; *Xia et al.*, 2004]. On the other hand, seismological inferences show that most earthquakes have rupture velocities around 80% of the shear velocity [*Heaton*, 1990] and that a fairly large fraction of all large (i.e., M > 7) continental strike-slip earthquakes that have been sufficiently well recorded and analyzed propagate with supershear velocities: the M 6.5 1979 Imperial Valley, California, earthquake [*Archuleta*, 1984; *Spudich and Cranswick*, 1984], the M 7.4 1999 Kocaeli (Izmit), Turkey, earthquake [*Bouchon et al.*, 2000, 2001], the M 7.2 1999 Duzce, Turkey, earthquake [*Bouchon et al.*, 2001], the M 8.1 2001 Kokoxili (Kunlun), Tibet, earthquake [*Bouchon and Vallée*, 2003; *Robinson et al.*, 2006; *Bhat et al.*, 2007; *Vallée et al.*, 2008; *Walker and Shearer*, 2009]; the M 7.9 2002 Denali Fault, Alaska, earthquake [*Ellsworth et al.*, 2004; *Dunham and Archuleta*, 2004; *Aagaard and Heaton*, 2004; *Dunham and Archuleta*, 2005], and the M 7.9 1906 San Francisco, California, earthquake [*Song et al.*, 2008].

[3] More recently, two independent numerical studies of rupture propagation on planar, finite width, strike-slip faults breaking the free surface of a homogeneous, linear elastic half-space demonstrate that supershear rupture propagation strongly modifies the nature of seismic radiation. Specifically, *Bizzarri and Spudich* [2008, hereafter referred to as BS08] simulated the spontaneous (in that the rupture velocity, $v_r$, is not a priori assigned, but is itself determined as part of the problem and it can vary through time), fully dynamic propagation of truly 3-D ruptures obeying different constitutive laws. BS08 showed that, for a linear slip-weakening (SW) friction law with a constant stress drop, for SW with thermal pressurization effects, and for rate- and state-dependent friction laws with thermal pressurization of pore fluids, the slip velocity at fault points where the rupture edge is traveling with a supershear speed has less high frequency content than that calculated at points where the rupture velocity is subshear. This holds also in the case of heterogeneous initial stress. This is consistent with 2-D analytical solutions for supershear cracks, which have stress and velocity fields that are less singular at the crack tip than those in subshear cracks [*Burridge*, 1973; *Andrews*, 1976]. They also analytically demonstrated that in a kinematic rupture model having a given heterogeneous slip distribution with spectra following $k^{-2}$ ($k^{-1.5}$) at high radial wave number $k$, a supershear rupture propagation produces far-field ground motions that have a Fourier amplitude spectrum (FAS) boosted by a factor $\omega$ ($\omega^{0.5}$) with respect FAS originating from a subshear rupture ($\omega$ is the angular frequency, $\omega = 2\pi f$, being $f$ the temporal frequency). The application of these amplifications to the spontaneous fault slip velocity FAS causes the supershear FAS to exceed the subshear FAS, suggesting that *S* wave ground motion pulses from supershear ruptures should be richer in high frequency than ground motion pulses from subshear ruptures, despite the diminution of the crack tip singularity caused by supershear propagation.

[4] In a complementary study of rupture propagation at constant speed on homogeneous faults, *Dunham and Bhat* [2008, hereafter referred to as DB08] showed that supershear ruptures having a straight rupture front generate not only shear Mach waves (as already revealed by 2-D steady state models [*Dunham and Archuleta*, 2005; *Bhat et al.*, 2007]), but also Rayleigh Mach waves, which interfere and lead to complex velocity and stress fields. Rayleigh Mach fronts, most evident in the fault-normal and vertical components of particle velocity on the free surface, do not attenuate with distance from the fault trace (in a homogenous, ideally elastic medium). DB08 also demonstrated that while high particle velocities are concentrated near the fault trace for subshear ruptures, in case of supershear ruptures they extend widely in the direction perpendicular to the fault trace. Additionally, they showed that when rupture velocity increases from subshear to supershear speeds, the dominant component of particle velocity changes from fault-normal to fault-parallel, as also shown by *Aagaard and Heaton* [2004].

[5] As a natural consequence of these studies the present paper has the following goals: (1) to systematically explore differences in the frequency content of ground motions from supershear and subshear spontaneous dynamic ruptures, (2) to study the effects on the Mach fronts of any incoherence of the rupture front (due to the rupture front curvature and to the temporal changes in $v_r$), (3) to extend the conclusions of DB08 to a more realistic case where the initial stress is heterogeneous, as in BS08, and (4) to determine whether any of the theoretical Mach pulse amplifications predicted by these papers are found in real ground motion data.

## 2. Statement of the Problem and Methodology

### 2.1. The Numerical Model

[6] We solve the elastodynamic equation in the absence of body forces for a linear elastic half-space containing a single planar fault governed by a prescribed fault constitutive law. The model geometry is shown in Figure 1. The medium is initially at rest and moves only in response to waves excited by the earthquake source. Among many different possibilities presented in the literature [see *Bizzarri and Cocco*, 2006; *Bizzarri*, 2009, and references therein], for sake of simplicity we restrict our analysis to the linear SW friction law, which prescribes that the magnitude $\tau$ of fault shear traction (the fault strength) linearly decreases from its maximum, yield (or static friction) level $\tau_u$ ( = $\mu_u \sigma_n^{eff}$ ) down to the kinetic, residual (or dynamic friction) level $\tau_f$ ( = $\mu_f \sigma_n^{eff}$) as the cumulative fault slip $u$ increases from zero up to the characteristic SW distance $d_0$ [*Ida*, 1972], which

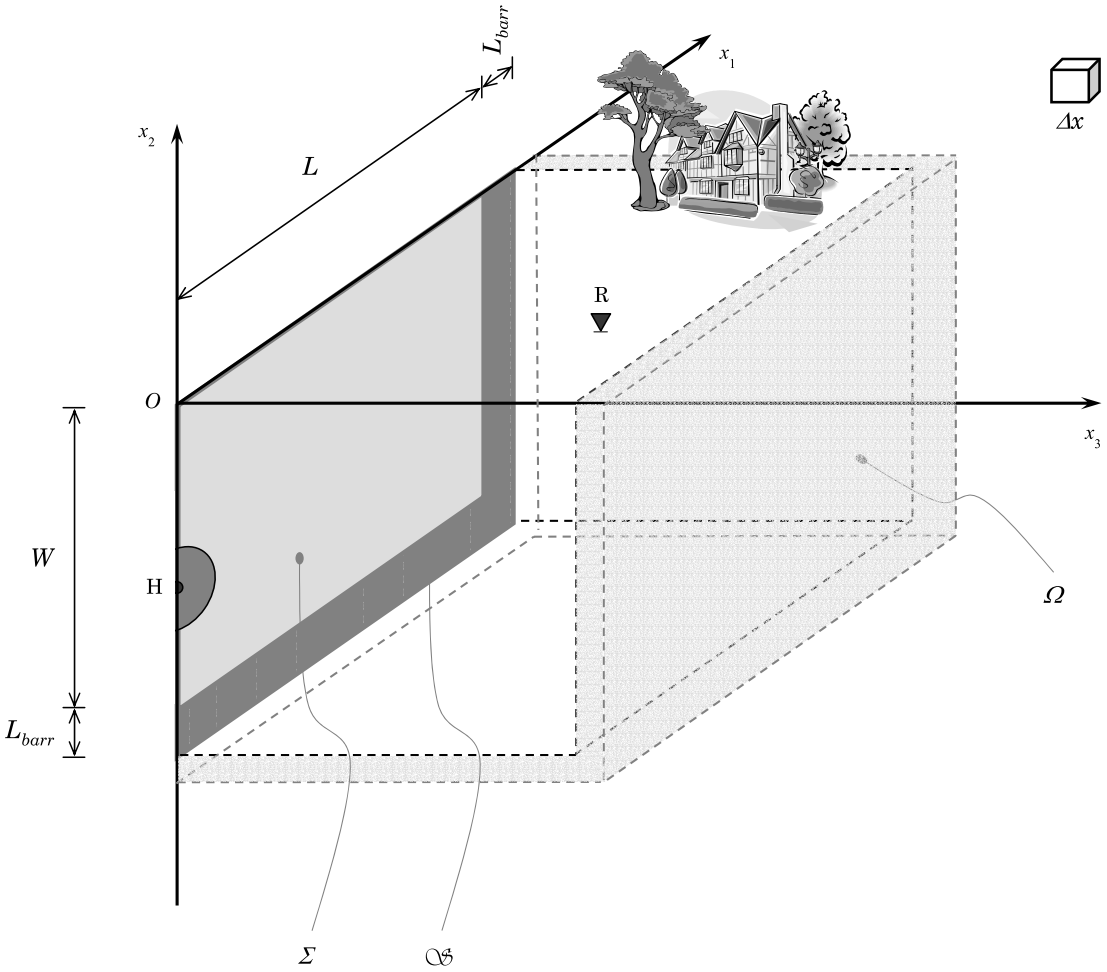


**Figure 1.** Geometry of the problem considered in this paper. Within the computational domain $\Omega$, the plane $\mathfrak{S}$ represents the fault, having hypocenter H. $\Sigma$, having aspect ratio $L/W$, is the portion of $\mathfrak{S}$ where the rupture can develop, before being arrested by the unbreakable barriers (dark gray) of length $L_{barr}$. Light gray indicates the points used for perfectly matched layers absorbing boundary conditions. R is a generic receiver on the free surface $x_2 = 0$. The grid spacing in all directions is $\Delta x$.

defines the breakdown (or cohesive) zone, after which $\tau$ remains constant:

$$\tau = \begin{cases} \tau_u - (\tau_u - \tau_f)\dfrac{u}{d_0} & , u < d_0 \\ \tau_f & , u \geq d_0 \end{cases} \quad (1)$$

where $u$ is the fault slip. This constitutive model is intentionally simple, and it should be regarded as a first approximation for how the fault strength evolves through time. Due to the fault geometry, uniform material properties, the no-opening condition, and the neglect of pore fluid pressure changes, the effective normal stress $\sigma_n^{eff}$ is constant in time.

[7] The problem considered here is spontaneous and it is solved numerically with a staggered grid, finite difference (SGFD) code, modified from the code by P. Favreau [*Favreau et al.*, 2002] and recently used by DB08. Since we are now mainly interested in the propagation of seismic waves in the body we prefer this method with respect to the conventional grid, finite difference (CGFD) code used by BS08 [see also *Bizzarri and Cocco*, 2005]; on the fault both are second-order accurate in time and both are second-order accurate in space. However, in the body surrounding the fault the SGFD code is fourth-order in space, while the CGFD code is second-order in space. The fault boundary condition is implemented with the staggered grid split-node (SGSN) method of *Dalguer and Day* [2007].

[8] The problem solved is 3-D, since both strike and dip components of physical observables (slip, slip velocity and shear traction) are nonzero and both depend on two spatial coordinates; i.e., rake rotation is allowed. Since the slip vector is not constrained to have only one nonzero component, the frictional dynamics are sensitive to the absolute level of stress [*Spudich*, 1992; *Bizzarri and Cocco*, 2005; *Dunham*, 2007]. The usual requirement of collinearity of the slip velocity and traction vectors is imposed.

[9] The SGFD method uses centered finite differences (except in the vicinity of the fault and boundaries) and thus has no intrinsic numerical dissipation. The highest frequency waves suffer from numerical dispersion and propa-

**Table 1.** Model Discretization and Constitutive Parameters

| Medium and Discretization Parameters | Value | |
|---|---|---|
| Lamé constants, $\lambda = G$ | 32 GPa | |
| Rayleigh velocity, $v_R$ | 3.184 km s$^{-1}$ | |
| $S$ wave velocity, $v_S$ | 3.464 km s$^{-1}$ | |
| Eshelby velocity, $v_E = \sqrt{2}v_S$ | 4.899 km s$^{-1}$ | |
| $P$ wave velocity, $v_P$ | 6 km s$^{-1}$ | |
| Mass density, $\rho$ | 2670 kg m$^{-3}$ | |
| Fault length, $L$ | 110 km | |
| Fault width, $W$ | 10 km | |
| Length of unbreakable barriers, $L_{barr}$ | 3 km | |
| Computational domain, $\Omega$ | Box that extends from 0 up to $x_{1end} = 11W + L_{barr}$ (= 113 km) along $x_1$, from $-W - L_{barr}$ (= −13 km) up 0 along $x_2$ and from 0 up to $x_{3end} = 5.5W$ (= 55 km) along $x_3$ | |
| Plane containing the fault, $\mathcal{S}$ | $\{\mathbf{x} \mid x_3 = x_3^f = 0\}$ | |
| Fault, $\Sigma$ | $\{\mathbf{x} \mid 0 \le x_1 \le L, -W \le x_2 \le 0, x_3 = x_3^f\} = \{\mathbf{x} \mid 0 \le x_1 \le 110$ km, $-10$ km $\le x_2 \le 0, x_3 = 0\}$ | |
| Spatial grid spacing, $\Delta x_1 = \Delta x_2 = \Delta x_3 \equiv \Delta x$ | 100 m | |
| Time step, $\Delta t$ | $2.5 \times 10^{-3}$ s | |
| Courant-Friedrichs-Lewy ratio, $\omega_{CFL} = v_S \Delta t / \Delta x$ | 0.0866 | |
| Frequency for spatial grid dispersion, $f_{acc}^{(s)} = v_S/(6\Delta x)$ | 5.77 Hz | |
| Coordinates of the hypocenter, H $\equiv (x_1^H, x_2^H, x_3^H) = (x_1^H, x_2^H, x_3^f)$ | (0, −7.3, 0) km | |
| **Fault Constitutive Parameters** | **Model A** | **Model B** |
| Magnitude of the initial shear stress, $\tau_0$ | 73.80 MPa | 63.88 MPa |
| Magnitude of the effective normal stress, $\sigma_n^{eff}$ | 120 MPa | 120 MPa |
| Static friction coefficient, $\mu_u$ | 0.677 ($\leftrightarrow \tau_u = 81.24$ MPa) | 0.677 ($\leftrightarrow \tau_u = 81.24$ MPa) |
| Dynamic friction coefficient, $\mu_f$ | 0.46 ($\leftrightarrow \tau_f = 55.20$ MPa) | 0.46 ($\leftrightarrow \tau_f = 55.20$ MPa) |
| Dynamic stress drop, $\Delta\tau_d = \tau_0 - \tau_f$ | 18.60 MPa | 8.68 MPa |
| Strength parameter, $S$ | 0.4 | 2 |
| Characteristic slip-weakening distance, $d_0$ | 0.8 m | 0.8 m |

gate at slower speeds than desired, leading to oscillatory dispersive signals trailing underresolved wavefronts. These features are most pronounced behind the shear and Rayleigh Mach fronts and should not be mistaken for actual signals.

### 2.2. Model Parameters

[10] The parameters adopted in this work are slightly modified with respect to those used in Southern California Earthquake Center (SCEC) benchmark problems [*Harris et al.*, 2009] and are summarized in Table 1. We consider an isolated, vertical, right-lateral, strike-slip fault $S$ (the plane $x_3 = 0$ in Figure 1), embedded in a Poissonian medium with homogeneous properties. Ruptures are nucleated from the hypocenter H by forcing expansion at constant speed (equal to half of the $S$ wave speed) by imposing a time-weakening friction within the nucleation patch (see equation (1) in DB08, with $A = 0.2$ m$^{-1}$ and $v_r = 1.732$ km s$^{-1}$). When the value of fault strength predicted by the slip-weakening law (1) is lower than that predicted by time-weakening friction the former takes over and the rupture becomes fully spontaneous. Readers can refer to *Bizzarri* [2010] for technical details and discussion. The rupture is allowed to propagate on the portion $\Sigma$ of $\mathcal{S}$, i.e., until it reaches the impenetrable fault borders (dark gray regions of Figure 1), where the value of $\tau_u$ is sufficiently high to prevent rupture propagation.

[11] The length of the fault, $L$, has been chosen in order to prevent the time series at a free surface receiver R $\equiv (x_1^R, 0, x_3^R)$ from being affected by stopping waves coming from unbreakable fault borders before the end of the signal emitted by the source propagating past the receiver. In general, denoting by $\langle v_r \rangle$ the spatially averaged rupture velocity over the distance $L - x_1^H$, the $P$ and $S$ stopping waves arrive at times greater than

$$t_{s_P}^R = \frac{L - x_1^H}{\langle v_r \rangle} + \frac{\sqrt{\left(L - x_1^R\right)^2 + \left(x_3^R\right)^2}}{v_P} \tag{2}$$

and

$$t_{s_S}^R = \frac{L - x_1^H}{\langle v_r \rangle} + \frac{\sqrt{\left(L - x_1^R\right)^2 + \left(x_3^R\right)^2}}{v_S} \tag{3}$$

respectively (the latter generalizes equation (4) of DB08; in previous equations, $x_1^H$ is the strike coordinate of the hypocenter and $v_P$ and $v_S$ are $P$ and $S$ wave velocities, respectively). Expressions (2) and (3) neglect the additional distance traveled from sources at nonzero depth, making these lower bounds. Note that our model includes stopping waves originating from the bottom of the fault ($x_2 = -W$), which are an essential part of the wavefield generated by rupture propagation on faults of finite width. We picked fault dimensions (i.e., $L$ and $W$) based on the theory described by *Dunham* [2007] to ensure supershear propagation speeds.

[12] An important limitation of our study is the use of a relatively large SW distance compared to what has been inferred from laboratory experiments, resulting in a slip-weakening region that is several hundreds of meters in extent. Consequently, the ruptures in our simulations are not particularly sensitive to stress heterogeneities at scales smaller than this (i.e., they do not exhibit rapid accelerations or decelerations at short wavelengths). This limits the

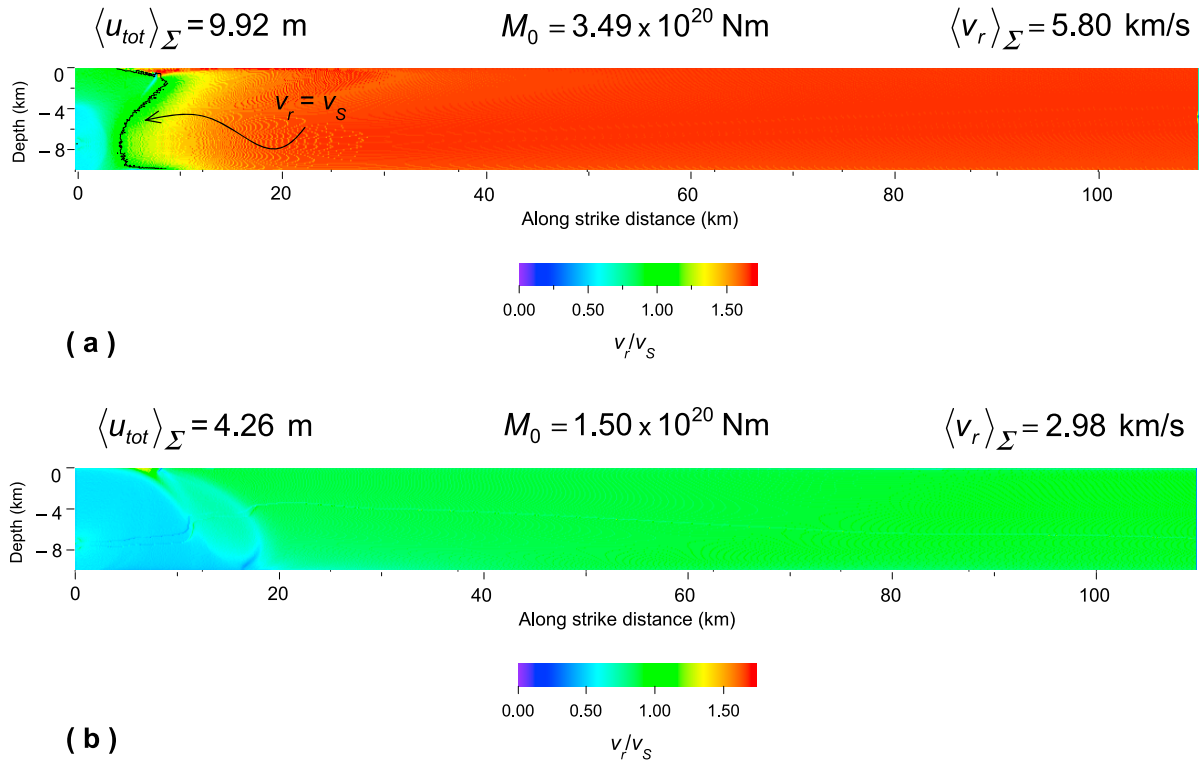


**Figure 2.** Local rupture velocity, $v_r$, normalized by $S$ wave velocity, on the fault plane for (a) homogeneous supershear rupture (model A) and (b) homogeneous subshear rupture (model B). Black line in Figure 2a corresponds to $v_r = v_S$ contour. We report the total seismic moment, $M_0$, and the spatial averages over the whole fault surfaces of the total cumulative fault slip and rupture velocity ($\langle u_{tot} \rangle_\Sigma$ and $\langle v_r \rangle_\Sigma$, respectively).

bandwidth of high frequency waves that are excited in our simulations, and forces coherence of the rupture process over spatial scales comparable to and less than the slip-weakening zone size. Hence, our simulations serve to demonstrate how a heterogeneous source process alters ground motion carried by Mach fronts, but are unable to characterize the very high frequency variability and incoherence that is likely present in natural earthquakes. We therefore caution that it is likely inappropriate to take from our results a definitive quantification of the degree to which ground motion amplitudes are reduced due to realistically heterogeneous propagation. However, the numerical limitations do not prevent us from identifying several reasons why Mach fronts might be far less coherent in nature than previous homogeneous models have suggested, and we are able to provide quantitative predictions regarding the spectral properties of ground motion from heterogeneous supershear ruptures.

## 3. Supershear and Subshear Ruptures on Homogeneous Faults

[13] In the first part of the paper we consider two homogeneous configurations (models A and B in Table 1), where the frictional properties are uniform over the whole region $\Sigma$. These homogeneous models serve as references with which we can compare later results from heterogeneous models (see sections 4, 5, and 6). The low value of the strength parameter ($S = (\tau_u - \tau_0)/(\tau_0 - \tau_f)$, for prestress $\tau_0$ [*Das and Aki*, 1977]) of model A ($S$ = 0.4) allows the rupture to accelerate up to supershear rupture velocities. The higher value of S in model B ($S$ = 2) impedes the supershear transition and forces the rupture to remain subshear (the average value of rupture velocity over the whole fault is $\langle v_r \rangle_\Sigma = 2.98$ km s$^{-1}$). The differences in $S$ between models A and B arise from differences in $\tau_0$; we keep $\tau_u$ and $\tau_f$ the same in both models. While this results in a factor of two larger dynamic stress drop for model A than model B (see Table 1), it seems more reasonable to assume that supershear propagation occurs in response to locally elevated values of $\tau 0$ than to assume it is caused by substantial differences in either static or dynamic friction coefficients. This perspective is supported by laboratory rupture experiments [*Xia et al.*, 2004], where rupture speed is controlled by changing the prestress level. A factor of two difference in particle velocities is consequently expected simply because of the larger dynamic stress drop in model A. Figure 2 shows the distributions of rupture speed $v_r(x_1,x_2)$ on the fault plane for the two models, defined as

$$v_r(x_1, x_2) = \frac{1}{||\nabla_{(x_1,x_2)} t_r(x_1, x_2)||}$$

where $t_r$ is the time at which the slip velocity at fault point $(x_1,x_2)$ first exceeds 1 mm s$^{-1}$, while movies of the time evolutions of the fault slip velocity are available in the

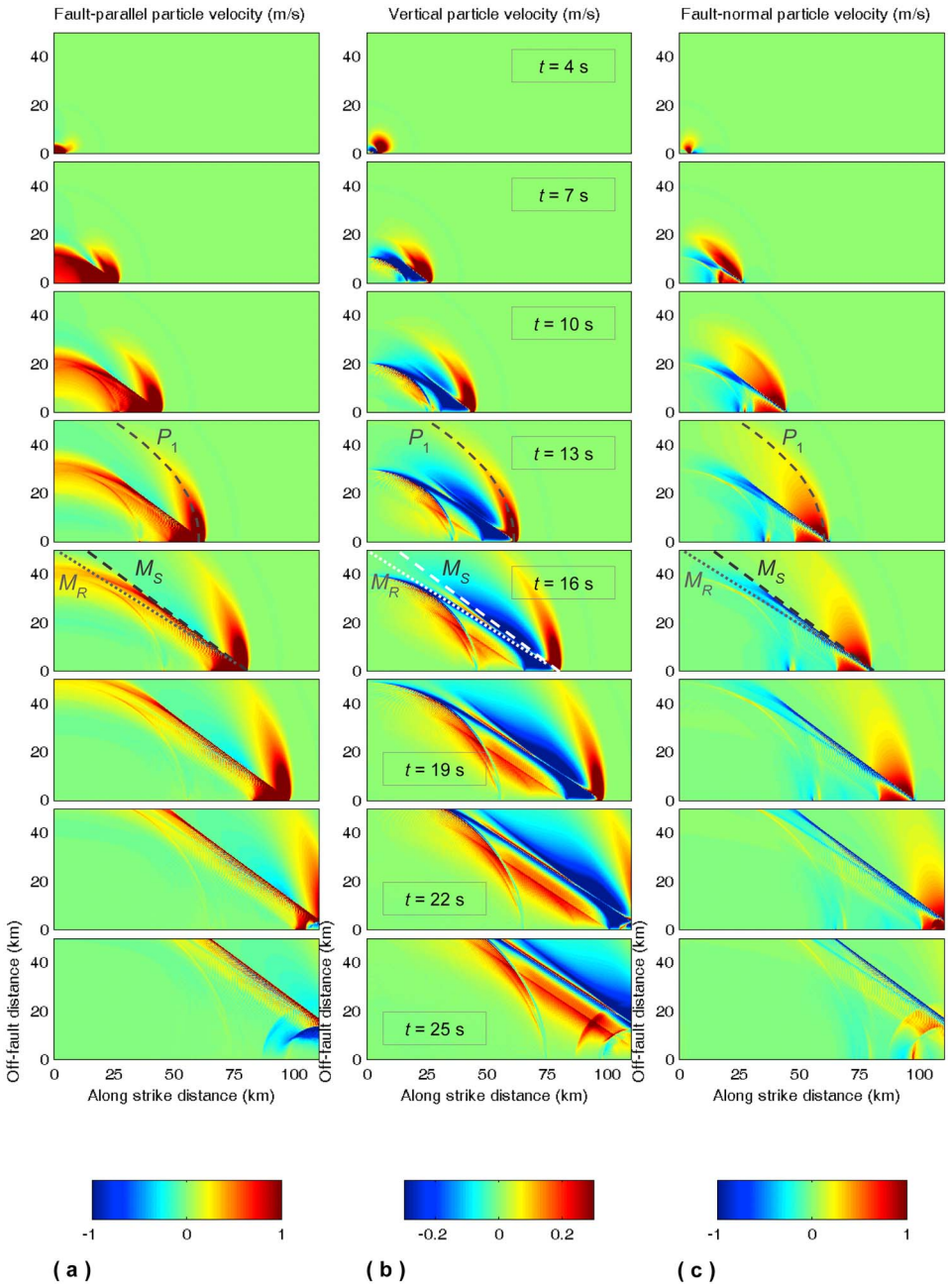


**Figure 3.** Snapshots at different times (indicated on the plots) of free surface particle velocity **V** for model A (with saturated color scale). $M_S$ and $M_R$ are the shear and Rayleigh Mach wavefronts, respectively, and $P_1$ denotes the first positive peak in particle velocity, associated with dilatational motion. Note in last two snapshots the stopping phases generated from unbreakable barrier at $x_1$ = 110 km. Numerical dispersion of high frequency waves is responsible for oscillations behind sharp wavefronts.

auxiliary material as Animations S1 and S2.[1] Soon after the imposed nucleation the crack tip travels at supershear speed in model A ($\langle v_r \rangle_\Sigma$ = 5.8 km s$^{-1}$, a value greater than the Eshelby speed $v_E = \sqrt{2} v_S$ = 4.9 km s$^{-1}$ [*Eshelby*, 1949]). As already demonstrated in earlier papers [e.g., *Bizzarri and Cocco*, 2005; BS08], the rupture velocity in the direction perpendicular to most slip remains subshear (see also Animation S1).

[14] In Figures 3 and 4 we follow the temporal evolution of the fault-parallel (Figures 3a and 4a, $V_1$), vertical (Figures 3b and 4b, $V_2$) and fault-normal (Figures 3c and 4c, $V_3$) particle velocities on the free surface, for models A and B, respectively. From Figure 3 we can clearly see that the fully dynamic, spontaneous supershear rupture exhibits both shear wave Mach fronts ($M_S$) and Rayleigh Mach wavefronts ($M_R$). The latter, which are more easily detect-

[1] Auxiliary materials are available in the HTML. doi:10.1029/2009JB006819.

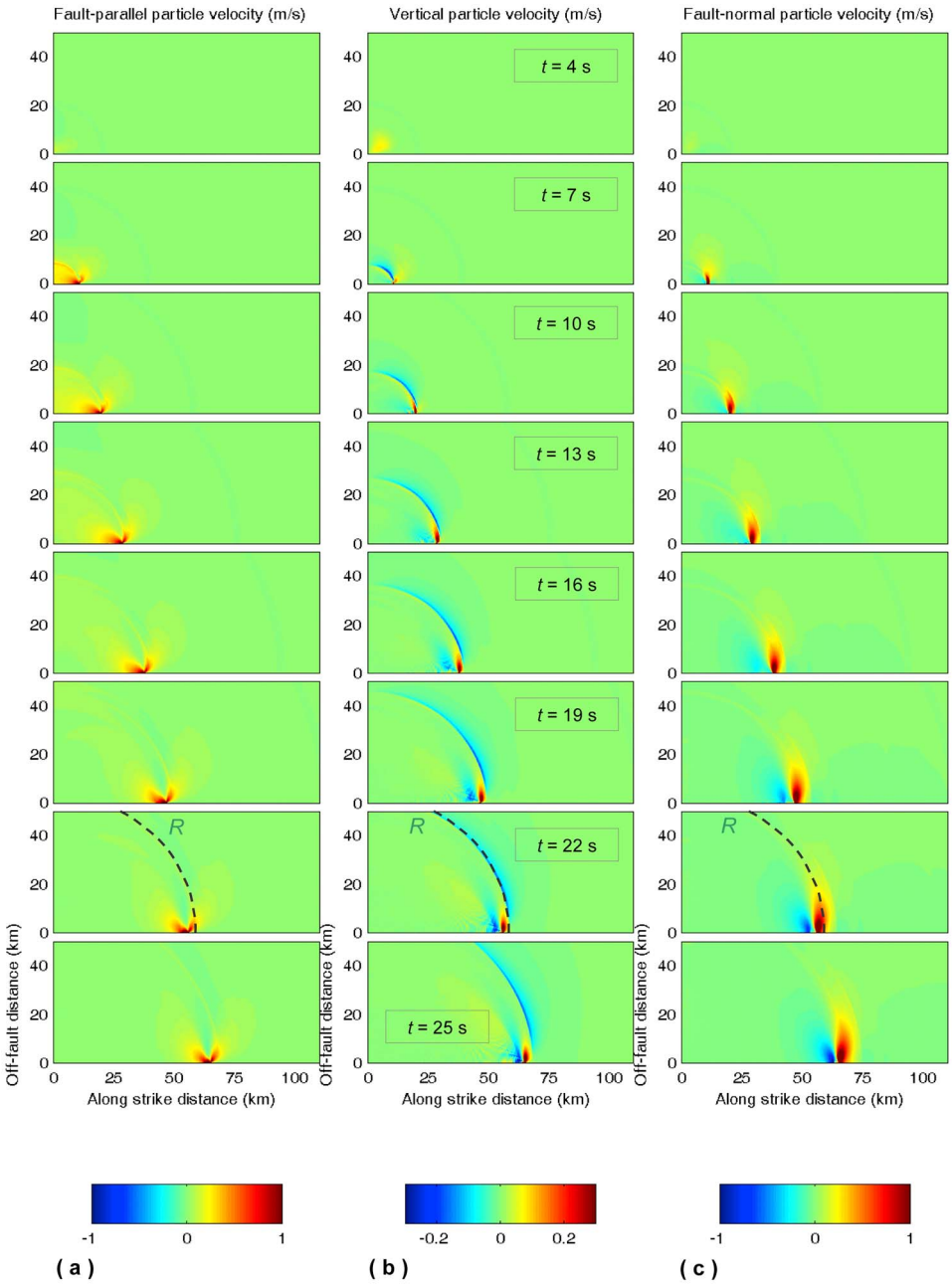


**Figure 4.** Same as Figure 3, but for model B. *R* denotes the Rayleigh wavefront.

able in the fault-normal and vertical components of **V**, is the weaker of the two. Both Mach fronts are quite sharp in the homogeneous case, though this is slightly obscured by the undamped numerical oscillations behind these wavefronts that arise from numerical dispersion. From Figure 3 we observe that the inclination of $M_S$ with respect to the $x_1$ axis (which is expressed as $\beta_S = \arcsin(v_S/v_r)$) is constant through time, suggesting that the rupture velocity is constant; this prediction is in agreement with our numerical calculation of $v_r$. These results basically confirm what DB08 found in their nonspontaneous model with a straight rupture front. In agreement with DB08, the comparison between Figures 3 and 4 confirms that in the steadily propagating homogeneous subshear case (Figure 4) **V** is significant only near the fault trace, while in the supershear case (Figure 3) large ground velocities extend to the end of the computational domain in the direction perpendicular to the fault.

[15] From the temporal evolution of wavefields emitted by the subshear rupture (Figure 4) we can see that the sharp, negative arcuate wavefront clearly visible in $V_2$ (marked as *R*) is the Rayleigh wavefront.

[16] In Figures 5 and 6 we plot the time evolution of the three components of normalized particle velocity at 8 receivers on the free surface, at the same distance along strike and equally spaced in the off-fault direction by 5 km. We have chosen a distance (50 km) from the hypocenter in the strike direction in order to be sure to capture all features of the well-developed rupture, such as the Mach wavefronts

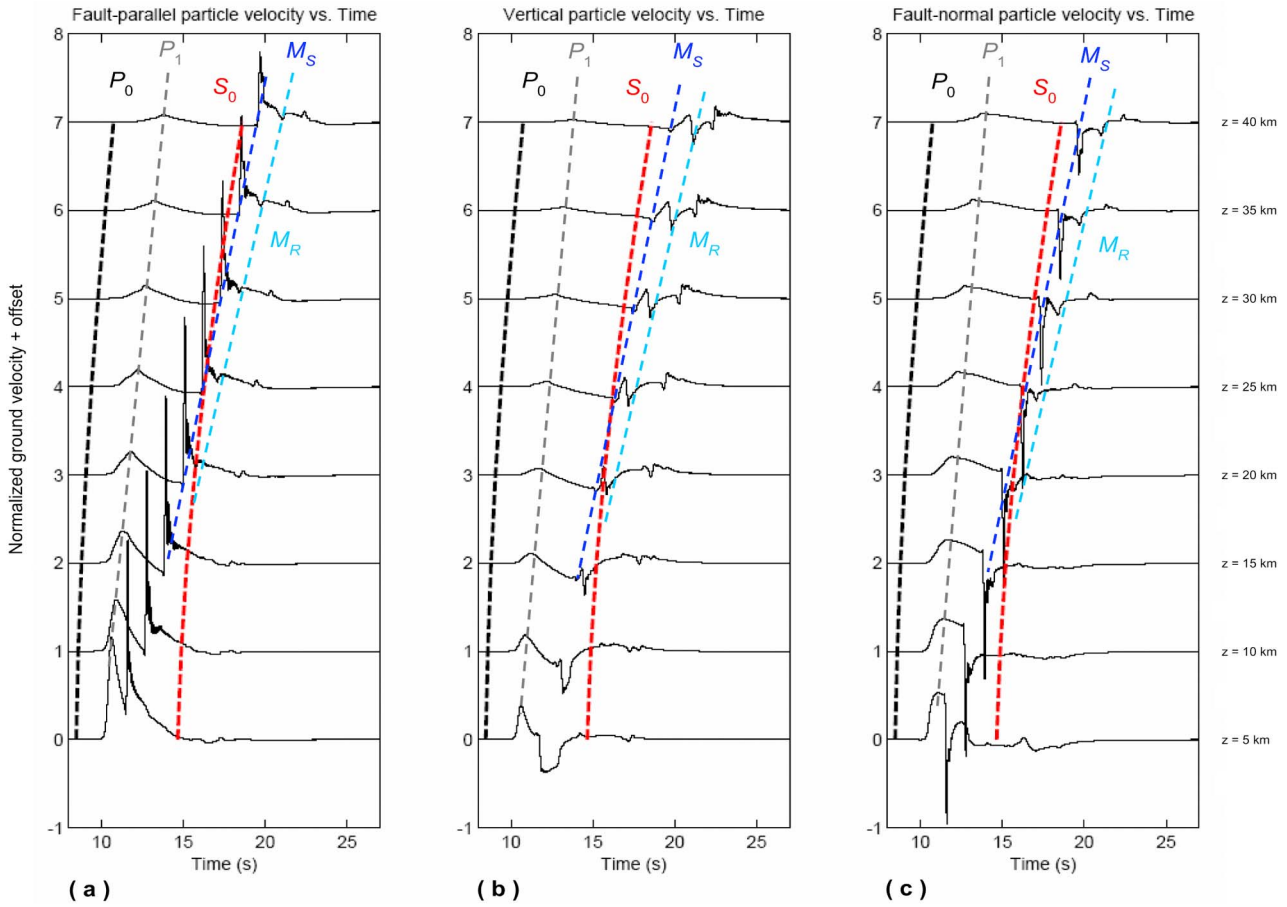


**Figure 5.** Time evolution, low-passed at 8 Hz, of normalized free surface particle velocity for model A at several receivers, all located 50 km along strike from the hypocenter and equally spaced by 5 km in the direction normal to the fault (the absolute location of each receiver is indicated, for each trace, to the right of Figure 5c). Velocity is normalized by the multiplier factor $G/(v_S\Delta\tau_d)$ and offset for $n$th receiver is $(n-1)$. $P_0$ and $S_0$ mark the theoretical arrival times of the direct $P$ and $S$ waves from the hypocenter, respectively. $M_S$ and $M_R$ indicate the shear and Rayleigh Mach fronts, respectively, and $P_1$ denotes the first positive peak associated with dilatational motions, as in Figure 3a. The stopping wavefronts are outside the time window considered here for all free surface receivers.

in the supershear case (and to minimize the potential effects of the imposed nucleation procedure). In agreement with DB08 we can see that, as the distance from the fault trace increases, the amplitude of particle velocity (especially $V_1$ and $V_3$) decreases faster in the subshear model compared to the supershear one in these models having fairly uniform rupture speed. While in (supershear) model A even at large distances from the fault there is significant ground motion, in (subshear) model B the signal is drastically attenuated at distances larger than about 20 km from the fault. Another interesting feature emerging from the comparison of Figures 5 and 6 is that in the supershear model $V_1 > V_2$ at most locations; on the contrary, in the subshear model the opposite is true (i.e., $V_1 < V_2$ at most locations). This result confirms the conclusions of *Aagaard and Heaton* [2004] and DB08.

[17] In the supershear model we have identified the shear ($M_S$) and Rayleigh Mach wave ($M_R$) arrivals (see Figure 5). To determine the shear Mach wave arrival time at an arbitrary free surface receiver R, we calculated the $S$ wave isochrones [*Bernard and Madariaga*, 1984; *Spudich and Frazer*, 1984] for that receiver, which are the contours on the fault of the $S$ wave arrival time function (sum of rupture time and $S$ wave travel time). An example of $S$ wave isochrones for the receiver located at $x_3 = 35$ km is reported in Figure 7a. There are two stationary points of the arrival time function (where the isochrone velocity is singular): a local minimum at $t = 18.43$ s (corresponding to the fault point (22.9, −4.25) km), which defines the arrival time of the shear Mach front, and a saddle point at $t = 18.62$ s (at (8.0, −6.45) km), which is another pulse consisting of $S$ wave energy radiated from the rupture front that can be seen in Figure 5b as the first local maximum in $V_2$ after the $M_S$ arrival. By definition, there is no information regarding the Rayleigh waves in the $S$ wave isochrones; however, we are able to pick the Rayleigh Mach front by looking at the time series (Figure 5). In general, $M_R$ corresponds to a local minimum in $V_2$ ($t = 18.93$ s for receiver at $x_3 = 35$ km) after $M_S$, and it arrives slightly after the big negative pulse in $V_3$.

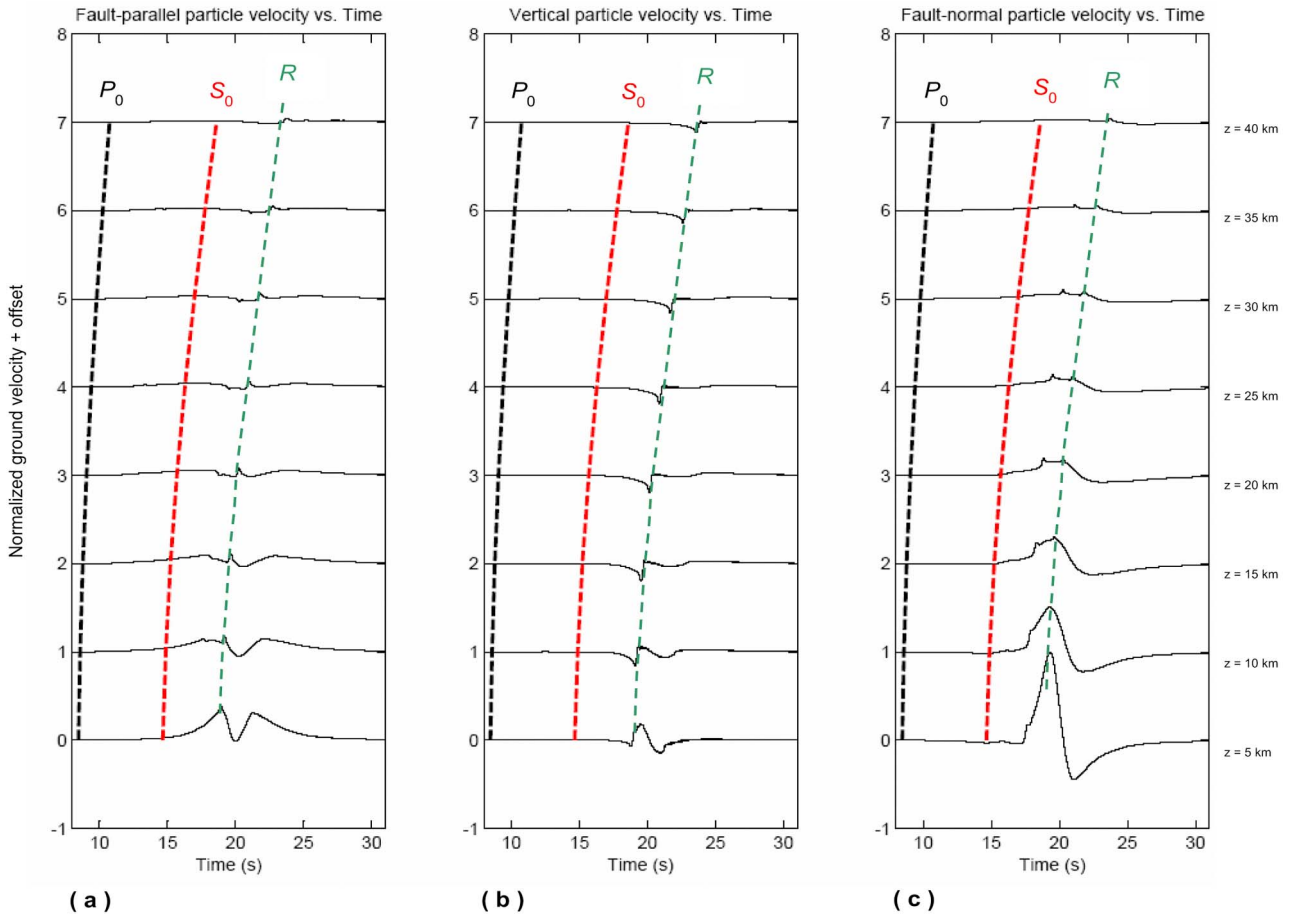


**Figure 6.** Same as Figure 5 but for model B. Also in this case the stopping wavefronts are outside the considered time window considered. *R* marks the Rayleigh wavefront.

[18] From the calculation of the isochrones for all receivers it emerges that, at this along strike distance, the shear Mach front is well developed away from the fault (i.e., all receivers have singular points in *S* wave isochrone velocity). This is not true for receivers located at smaller strike distances (i.e., closer to the hypocenter), where the shear Mach front is not developed on the free surface; for example, at the strike distance of 9 km only a few receivers close to the fault experience the arrival of the $M_S$ and $M_R$ pulses.

[19] We indicate these wavefronts on a time snapshot (at $t$ = 16 s) of the fault-normal component of particle velocity on the free surface (Figure 7b), again for the supershear model. In this plot $P_1$ denotes the first maximum in $V_3$ (well distinguishable in all components of **V**; see Figure 5). It is a local maximum on all components and is consistent with the "dilatational motion" described by *Dunham and Archuleta* [2005, Figure 2d], which becomes more pronounced as rupture velocity approaches the *P* wave speed (due to directivity), and which is most evident on the fault-parallel component (as expected for a *P* wave propagating nearly parallel to the fault). The dashed line marks the shear Mach front ($M_S$), which is followed by the Rayleigh Mach front ($M_R$). Both Mach fronts originate at the rupture front, which intersects the free surface at approximately 8 km at this time, but have a different inclination with respect to the fault, indicating that they advance in the direction normal to the Mach front at different speeds.

## 4. Introduction of Shear Stress Heterogeneities

[20] It is well known that in the near-surface zone (top 3 km) seismic velocities are typically lower than at depth, and seismic attenuation is typically higher. There is empirical evidence that slip in the near-surface zone radiates less ground motion than does deeper slip [e.g., *Campbell and Bozorgnia*, 2008]. One proposed explanation is that the upper part of the fault is velocity strengthening. Thus, in a realistic model of the near surface zone, rupture near the free surface zone would be attenuated, and we would arguably see less pronounced free surface effects than we have observed in the two models discussed in the previous section. Moreover, seismological observations suggest that the complex variation of the rupture velocity during an earthquake, including acceleration and deceleration phases, affects the radiated high-frequency ground motion [*Madariaga*, 1983; *Spudich and Frazer*, 1984; *Vallée et al.*, 2008].

[21] The source of radiation complexity in real-world events is not yet precisely known. However, we now consider a model (model C) which has a heterogeneous initial shear stress consistent with a specified power spectral density (PSD). Specifically, we first generate a 2-D array that

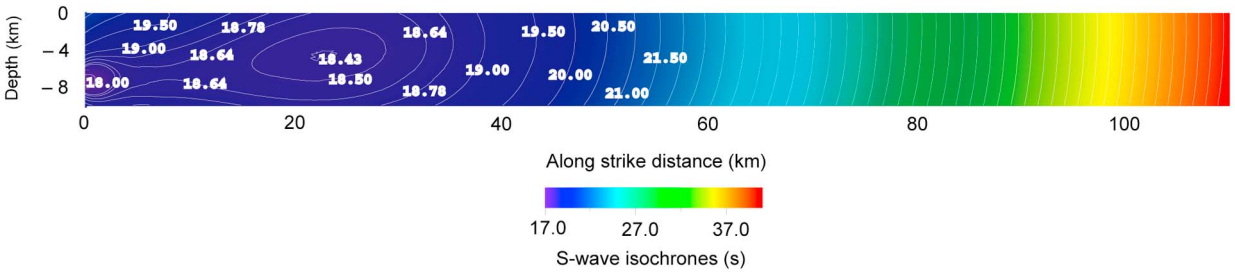


( a )

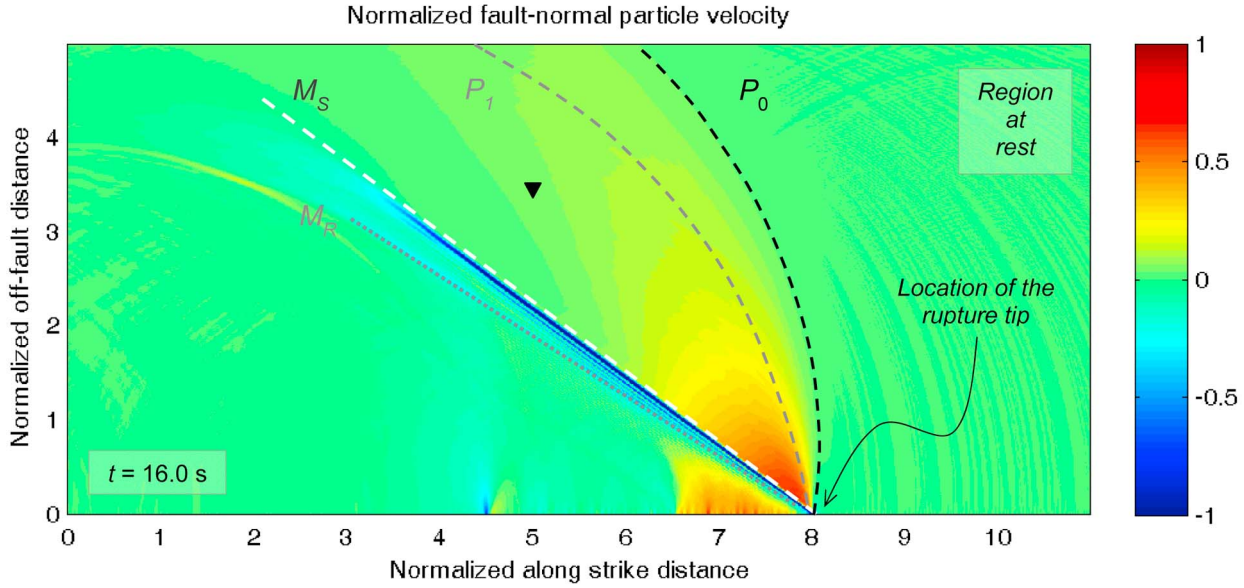


( b )

**Figure 7.** (a) *S* wave isochrones for model A for a free surface receiver located at $(x_1, x_3) = (50,35)$ km. (b) Snapshot at $t = 16$ s of the fault-normal component of particle velocity with major wavefront arrivals marked. Distances and velocity are normalized by means of the multiplicative factors $1/W$ and $G/(v_S \Delta\tau_d)$, respectively. Black inverted triangle marks receiver for isochrone calculation in Figure 7a.

covers all grid points on the fault composed of random numbers uniformly distributed between −1 and 1 (i.e., white noise). Then we multiply the Fourier transform of this distribution by $\sqrt{P(k)}$, where $P(k)$ is the PSD of the form

$$P(k) = B/k^{2+2H} \tag{4}$$

where $B$ is a normalization factor, $k$ is the radial wave number (i.e., the magnitude of the 2-D wave number vector $\mathbf{k}$, $k = \|\mathbf{k}\| = \sqrt{k_1^2 + k_2^2}$ for horizontal and vertical wave numbers $k_1$ and $k_2$, respectively) and $H$ is the dimensionless Hurst exponent [e.g., *Mai and Beroza*, 2002, equation (A11)]. In contrast to other studies, we take the perspective that stress is heterogeneous at all scales and we consequently do not introduce a correlation length into the model. In equation (4) we set $B = 1.4212 \times 10^5$ MPa$^2$ km$^2$ and $H = 0$, which gives a $k^{-1}$ distribution (compare equation (B12) of *Frankel and Clayton* [1986]) and which corresponds, in the static limit [*Andrews*, 1980], to the "$k$ square" model [*Herrero and Bernard*, 1994] in slip at high wave numbers. This makes sense since inversions of ground motion data show that slip functions of earthquakes have a random self–similar structure and the 2-D Fourier transform over the fault plane of slip is proportional to $k^{-2}$ [e.g., *Berge-Thierry et al.*, 2001, and references therein].

[22] We gradually remove power from wavelengths $\lambda$ between $3\Delta x$ and $6\Delta x$ ($\Delta x$ is the grid spacing) using a half-cosine taper in the wave number domain, and we assign no power to wavelengths below $3\Delta x$. The inverse Fourier transform of the obtained distribution is the heterogeneity in stress, $\Delta\tau^{(het)}$. This heterogeneity is added to a uniform reference initial stress field, $\tau_0^{(ref)} = 65.62$ MPa (an intermediate value between models A and B), so that $\tau_0^{(C)} = \Delta\tau^{(het)} + \tau_0^{(ref)}$. The upper yield stress is also heterogeneous, $\tau_u^{(C)} = \Delta\tau^{(het)} + \tau_u^{(ref)}$, where $\tau_u^{(ref)}$ is the value of $\tau_u$ of in previous models A and B. On the contrary, $\tau_f$ is constant (and equal to its value in previous homogeneous models). In

this way we obtain a stress drop distribution with the desired PSD (4). Moreover, the dynamic stress drop, $\Delta\tau_d$ ($=\tau_0-\tau_f$), the breakdown stress drop, $\Delta\tau_b$ ($=\tau_u-\tau_f$), and the strength parameter, $S$, are all heterogeneous. On the contrary, the strength excess ($\tau_u-\tau_0$) is constant, preventing the nucleation of the rupture at points other than H. The average value of the strength parameter is $S^{(ref)}=1.5$. All other parameters are the same as in models A and B (Table 1). We note that the average value of $\Delta\tau_d$ is intermediate between that pertaining to models A and B ($\Delta\tau_d^{(C)}=10.42$ MPa); moreover, the average value of $\Delta\tau_b$ is the same as in previous models A and B.

[23] The imposed initial shear stress in $\Sigma$ for model C is shown in Figure 8a; its 2-D and 1-D spectra are plotted in Figures 8b and 8c, respectively. The root mean square of $\Delta\tau^{(het)}$ is 20.09 MPa. Note, however, that this statistical measure depends on the minimum wavelength included in the model, and that this value is obtained for a distribution resolved with grid spacing $\Delta x=100$ m. We finally mention that the present implementation of heterogeneities does not account for the differences of physical properties with varying confining pressure and temperature (i.e., with varying depth).

## 5. Results for Heterogeneous Initial Stress

[24] Due to the heterogeneous value of the $S$ parameter, the distinction of the two speed regimes of propagation is not so strong as it was for previous models A and B; model C is, on average, supershear (see Figure 8d) but exhibits some subshear patches (the movie of the time evolution of the fault slip velocity is available as Animation S3). Unlike models A and B, which have extremely distinct stopping phases because the rupture is forced to halt abruptly along a vertical line (the barrier located at the end of the fault in the strike direction), model C is characterized by a gradual, spontaneous (and more realistic) cessation of slip at various locations (i.e., it stops at different times and distances along strike for each depth); when the rupture propagates into fault patches with negative stress drop (i.e., stress increase), it stops gradually. It is apparent that in this case the event size was not predictable a priori (i.e., before running the simulation). Model C represents an interesting example of how artificial it probably is to stop ruptures so abruptly at the end of the fault, as we have done in the homogeneous simulations. While stopping phases have been observed in some earthquakes (e.g., 2004 Parkfield [*Shakal et al.*, 2005]), they do not appear to be as sharp as homogenous simulations would predict.

[25] Results for the heterogeneous model essentially confirm what we see in homogeneous models, in particular, the two Mach fronts still appear (Figure 9). The presence of shear Mach waves is also confirmed by $S$ wave isochrone calculations (Figure 10a). Model C is an example of an earthquake that has enough regions experiencing supershear propagation to emit Mach pulses. By comparing Figures 10a and 7a we note that isochrones are complicated by stress heterogeneities. The same is true for the wavefields (compare Figures 9 and 3); the complications in wavefronts are evident in all components of ground velocity, especially in the vertical component. As in homogeneous model A, model C reveals that amplitudes at the dilatational wavefront $P_1$ die away with increasing fault-normal distance much faster than those at the Mach fronts. In Figure 10b we compare the time evolution of $\mathbf{V}$ for models A and C at the free surface receiver located at $(x_1,x_3)=(50,35)$ km (the station shown in Figure 7). In general, we can see that the time series of the heterogeneous case are slightly delayed with respect to the homogeneous one (they are not in phase); peaks associated with the dilatational motion ($P_1$ in Figure 10b) are at $t=13.30$ s for model A and at $t=14.01$ s for model C. In Figure 10b we have also indicated, for both models, the times at which $S$ wave isochrones hit the free surface and the bottom edge of the fault. We do this because when an isochrone hits a boundary a pulse is generated, since at that time its length changes discontinuously. In turn this causes the ground displacement to change discontinuously (ground displacement at time $t$ is a line integral of various quantities along the isochrone for time $t$) and this ultimately leads to the generation of a velocity pulse.

[26] Both models A and C also clearly exhibit the presence of the shear Mach front ($M_S$, which is not so strong on vertical, but very clear on the horizontal components of $\mathbf{V}$) and the Rayleigh Mach front ($M_R$, which is two sided in $V_2$ and less pronounced on the other two components of $\mathbf{V}$. As suggested by the local minima of the $S$ wave isochrones (Figures 7a and 10a), $M_S$ starts at $t=18.43$ s for the homogeneous model and at $t=19.20$ s for the heterogeneous one (Figure 10b).

[27] One important thing emerging from Figure 10b is that the amplitudes of the peaks of $\mathbf{V}$ are reduced in the heterogeneous model (C) with respect to those of homogeneous model (A). These conclusions hold also for other receivers on the free surface.

[28] Another important result from Figure 10b is that the shear Mach front is less coherent in model C than in model A. One source of incoherence is the variability in rupture front history (which is apparent from Figure 10a); the irregularity of the rupture front history causes the presence of several local minima in the $S$ wave isochrones (i.e., locations at which the $S$ wave isochrone velocity is singular), each of these points of stationary phase which yield a shear Mach pulse. To quantify this, we plot in Figure 11a histogram of the local minima of the arrival time function for model C; this is done for the same receiver considered in Figure 10. To determine the minima we first identify fault patches where $S$ wave isochrone velocity is singular and then we found the local minimum of the arrival time function in each patch. Each minimum is determined by considering the lowest value of the arrival time function of the first four neighboring values in the two directions (we therefore do not consider a minimum if it is located at the fault boundaries). While in the case of model A there is only one local minimum (at $t=18.43$ s, as previously noted), in the case of model C several minima appear and they are spread out over a time interval one second long. In the histogram in Figure 11a we can clearly see two peaks, one corresponding to the beginning of the $M_S$ wavefront ($t=19.20$ s) and the other to the time when the $S$ wave isochrones hits the free surface ($t=19.64$ s).

[29] Further incoherence in the Mach fronts arises from differences in slip velocity histories at different points on the fault, relative to the slip velocity history at the location of the isochrone minimum in each model, which we denote as

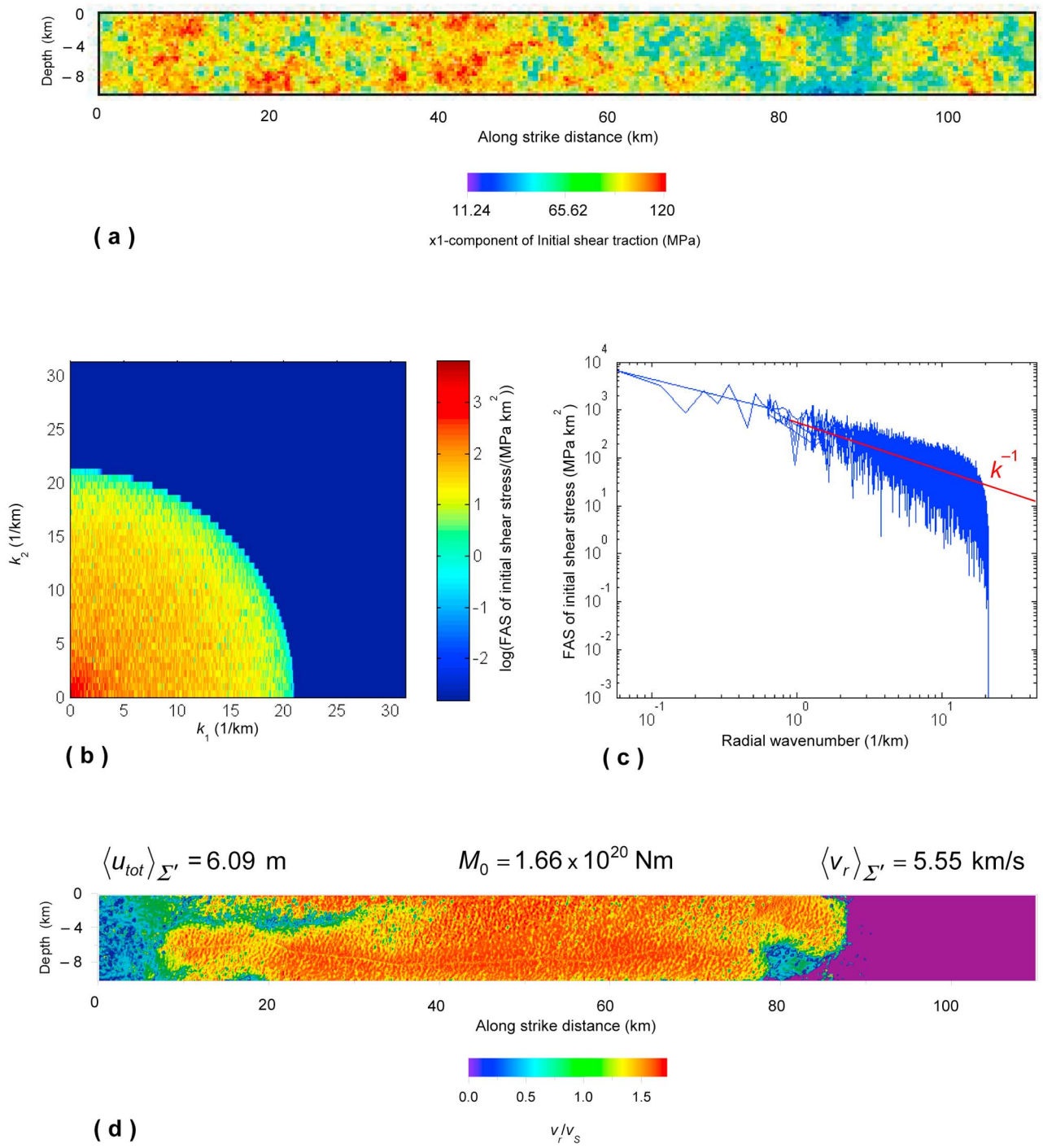


**Figure 8.** (a) Along strike component of initial shear stress for heterogeneous model C. (b) Fourier amplitude spectrum (FAS, i.e., absolute value of discrete Fourier transform) of initial shear stress, as a function of the horizontal ($k_1$) and vertical ($k_2$) wave numbers. (c) Same as Figure 8b but as a function of the radial wave number ($k = \sqrt{k_1^2 + k_2^2}$). (d) Distribution of $v_r/v_S$ for model C. The total seismic moment, $M_0$, and the spatial averages (over the fractured portion of the fault surface $\Sigma'$) of the total cumulative fault slip and rupture velocity are reported at the top of Figure 8d.

the reference point $(x_1^*, x_2^*)$. To quantify these spatial variations of $v$, for all fault points $(x_1, x_2)$ defined over a grid 0.5 km spaced in the two directions (i.e., every 5 fault nodes), we calculate the normalized cross correlation $C$ between slip velocity time histories as a function of the radial distance $r$ separating each of the fault points from the reference fault point ($r = \sqrt{(x_1 - x_1^*)^2 + (x_2 - x_2^*)^2}$) and azimuth angle $\varphi$

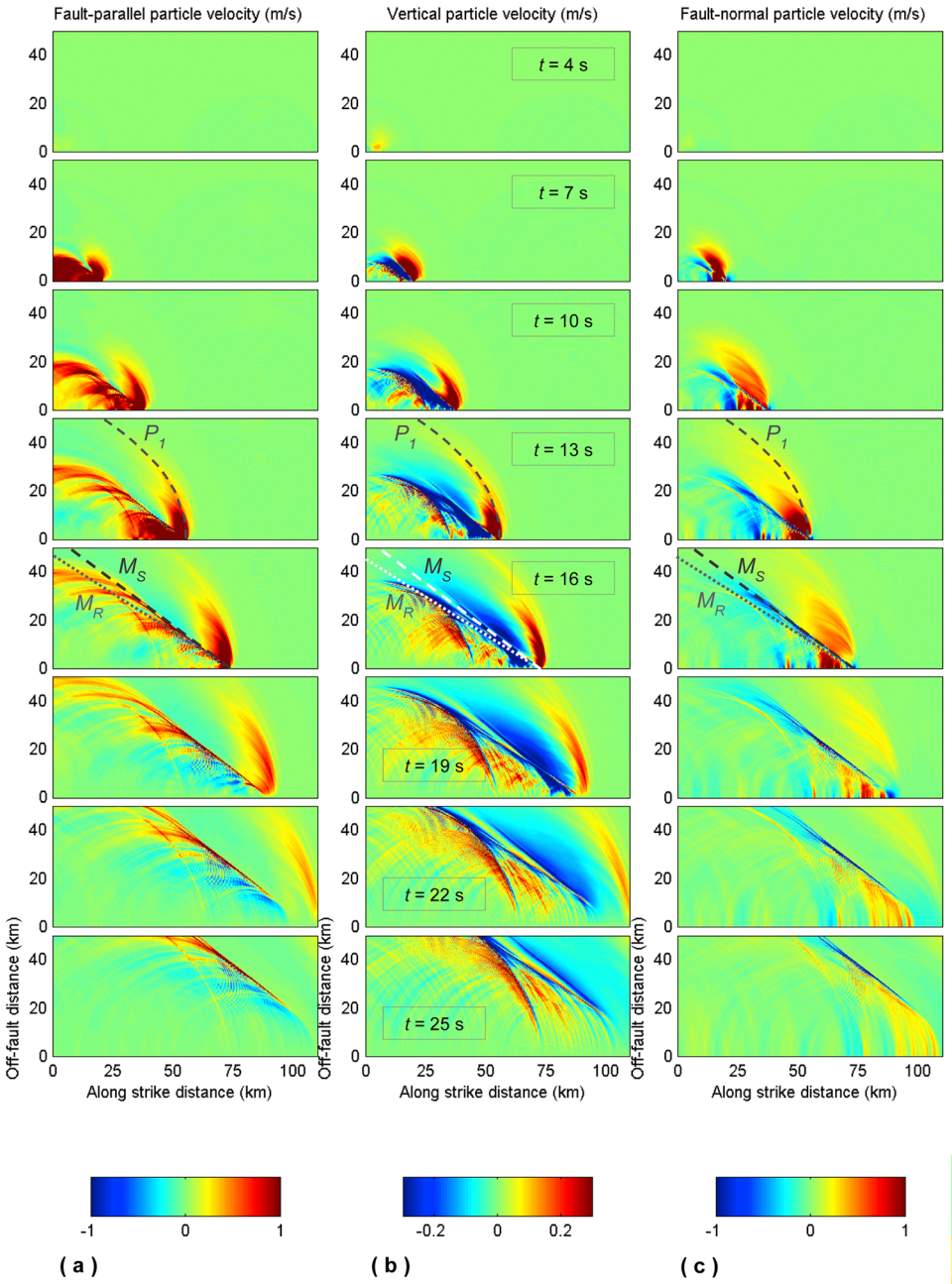


**Figure 9.** Same as Figure 3 but for model C. The shear ($M_S$) and Rayleigh ($M_R$) Mach fronts are not obscured by the presence of heterogeneities in the initial shear stress.

($\varphi$ = arctg2[$(x_2^* - x_2)/(x_1^* - x_1)$], where arctg2[] is the four quadrants inverse tangent):

$$C(r,\varphi) = \frac{\int_0^T v^{[lp]}(x_1^*, x_2^*, t_r(x_1^*, x_2^*) + t')dt' \int_0^T v^{[lp]}(x_1, x_2, t_r(x_1, x_2) + t')dt'}{\sqrt{\int_0^T \{v^{[lp]}(x_1^*, x_2^*, t_r(x_1^*, x_2^*) + t')\}^2 dt'} \sqrt{\int_0^T \{v^{[lp]}(x_1, x_2, t_r(x_1, x_2) + t')\}^2 dt'}} \quad (5)$$

In equation (5) the integrals are over a time window of duration $T = 5$ s after the rupture front arrival time, $t_r(x_1,x_2)$) and the superscripts $[lp]$ indicate that the fault slip velocity time series have been low passed at 8 Hz to remove numerical oscillations due to dispersion in the numerical method. The reference fault point is the point closest to the

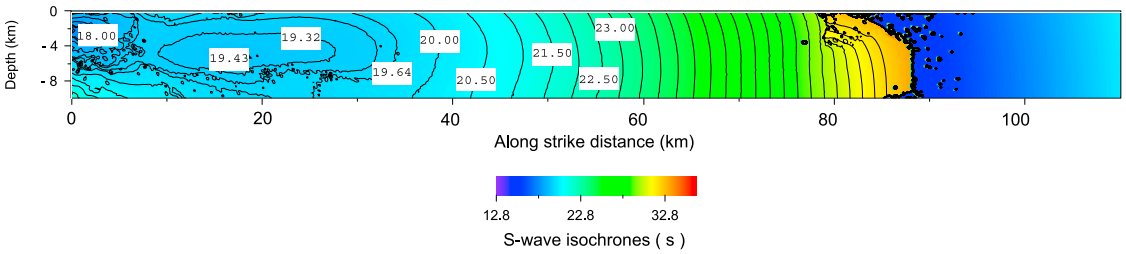


( a )

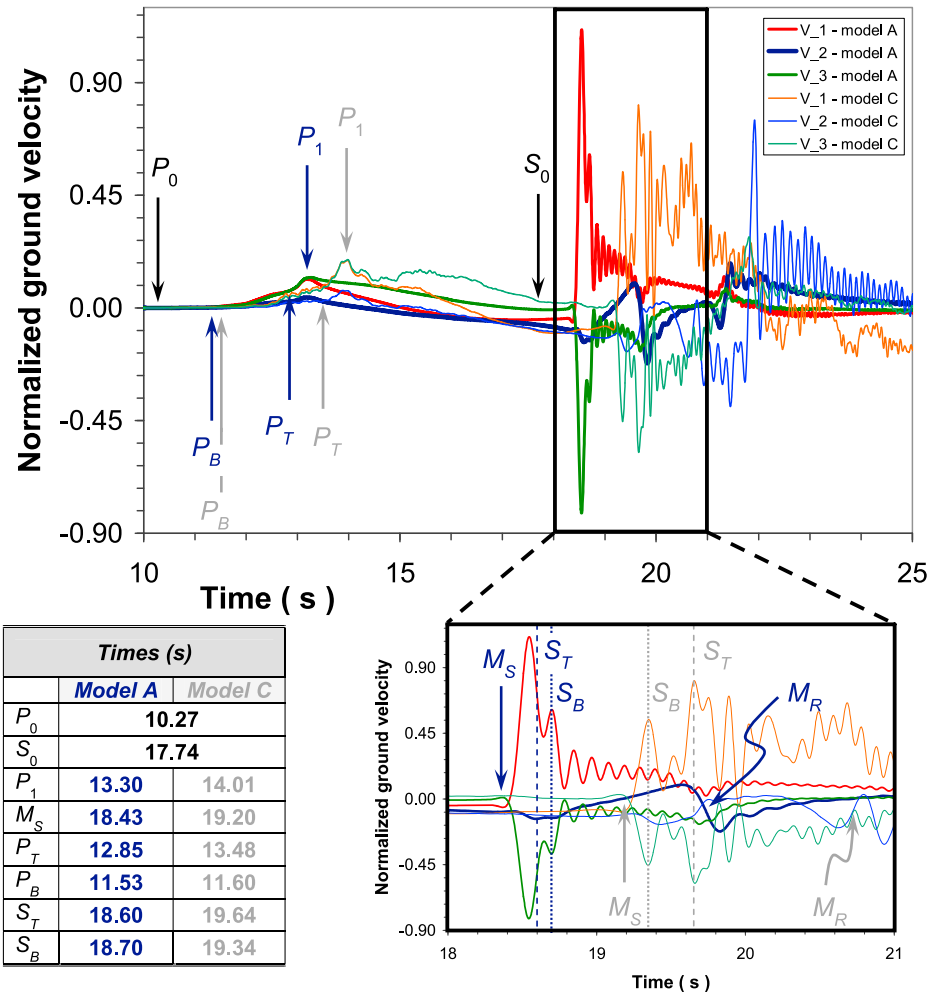


| Times (s) | | |
|---|---|---|
| | Model A | Model C |
| $P_0$ | 10.27 | |
| $S_0$ | 17.74 | |
| $P_1$ | 13.30 | 14.01 |
| $M_S$ | 18.43 | 19.20 |
| $P_T$ | 12.85 | 13.48 |
| $P_B$ | 11.53 | 11.60 |
| $S_T$ | 18.60 | 19.64 |
| $S_B$ | 18.70 | 19.34 |

( b )

**Figure 10.** (a) *S* wave isochrones for a free surface receiver located at $(x_1, x_3) = (50,35)$ km (the same as that of Figure 7a). (b) Time histories, with a zoom of the time interval [18,21] s, of the free surface velocity **V** for homogeneous (model A, thick lines) and heterogeneous (model C, thin lines) supershear ruptures at this free surface receiver. In Figure 10b, and in its zoomed part, the principal fronts are indicated (in blue for model A and in gray for model C). In addition to direct *P* and *S* wave arrivals from H ($P_0$ and $S_0$, respectively) and to the first peaks associated to the dilatational motion ($P_1$), we also indicate the times at which *P* and *S* wave isochrones hit the top ($P_T$ and $S_T$, respectively; they are $P_{B1}$ and $S_{B1}$ in the work by *Bernard and Baumont* [2005]) and the bottom of the fault ($P_B$ and $S_B$, respectively; they are $P_{B3}$ and $S_{B3}$ in the work by *Bernard and Baumont* [2005]). Times are reported in the tabulation. Normalization of $V_k$ is the same as in Figures 5 and 6.

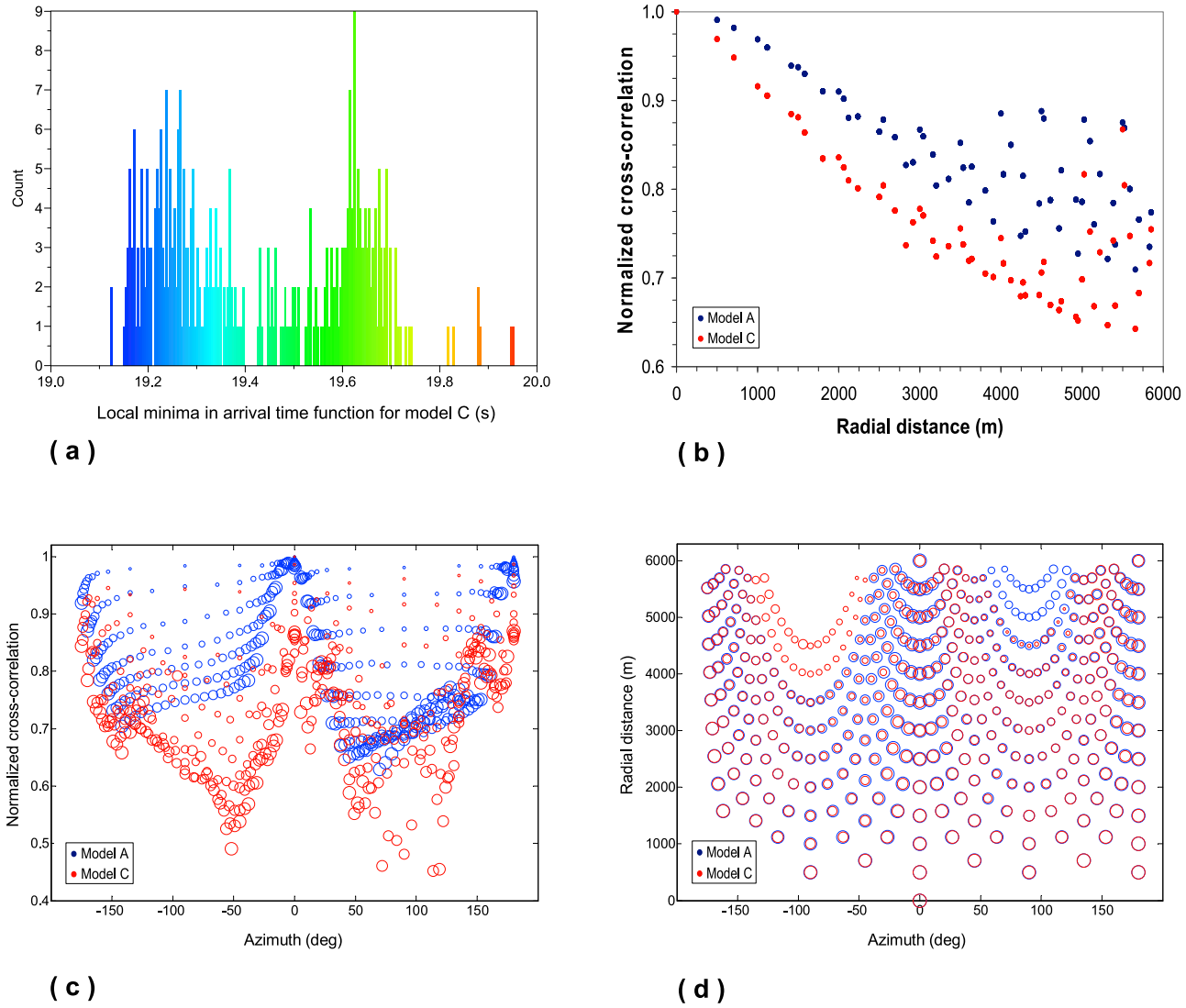


**Figure 11.** (a) Histogram of local minima in arrival time function for model C at the same receiver considered in Figure 10. (b) Azimuthally averaged normalized cross correlation as a function of radial distance (see section 5 for details). (c and d) Unaveraged normalized cross correlation as a function of radial distance and azimuth angle for model A (blue circles) and model C (red circles). In Figure 11c the circle size is proportional to radial distance $r$ (the biggest circle corresponds to $r = 5.85$ km), while in Figure 11d it is proportional to the normalized cross correlation (the biggest circle corresponds to $C = 1$). In Figures 11c and 11d positive (negative) azimuth angles identify a fault point located above (below) the point of absolute minimum of $S$ wave isochrones (i.e., closer (farther) to the free surface.

minimum of $S$ wave isochrones for the receiver considered in Figures 7a, 10, and 11 ($(x_1^*,x_2^*) = (24,–4)$ km for model A and $(x_1^*,x_2^*) = (18,–5)$ km for model C). We consider radial distances smaller than 6 km, since these points are the ones that can contribute to the Mach pulses of Figure 10b. The normalization of $v^{[lp]}$ by its Euclidean length and the positivity of $v$ ensure that $C \in [0,1]$.

[30] In Figure 11b we compare the behavior of $C$ as a function of radial distance, averaging values of $C$ for the same value of $r$. It emerges that $C(r)$ decays faster in model C than in model A: for model C the slope roughly is $–0.081$ km$^{-1}$, while that of model A roughly is $– 0.058$ km$^{-1}$. In Figures 11c and 11d we plot the cross correlation as defined in equation (5) as a function of $r$ and $\varphi$ (i.e., without averaging); blue circles refer to model A, while red circles to model C. In Figure 11c size of the circles is proportional to the radial distance; in Figure 11d it is proportional to the value of $C$. From Figure 11d we can see that for the same values of $r$ and $\varphi$ the cross correlation is lower in model C than in model A, confirming the result of Figure 11b. Moreover, Figure 11d indicates that for both models A and C, for small radial distances ($r < 1.5$ km), there is little evidence of azimuthal variation of $C$. On the contrary, for larger $r$, there appears to be fairly strong azimuthal dependence of $C$; the highest cross correlation is reached at $\varphi = 0°$ and at $\varphi = \pm 180°$. This indicates that points at constant depth (i.e., in the in-plane direction) are most correlated and this is justified by the fact that fault slip velocity histories

have two big peaks, one associated to the rupture front traveling at a supershear speed and the other one caused by the free surface reflection; these two peaks are coincident at the free surface and they are separated by a distance that varies with depth, but is little influenced by the propagation along strike (see Animations S1 and S3). Moreover, from Figure 11d, $C$ appears to be low for $\varphi$ between $\pm 40°$ and $\pm 130°$ and its minimum appears to be around $\varphi = \pm 65°$ (i.e., mixed mode behavior). This result recalls the observation of BS08 that the weakest singularity occurred for points that were mixed mode.

[31] In addition to the stronger dependence of $C$ on $r$ in model C with respect to that in model A, from Figure 11c we can also see that the in heterogeneous model $C$ exhibits a higher dependence on $\varphi$ than in homogeneous model. Again, we see that $C$ is minimum at the points of the fault where motion is mixed mode.

## 6. Sensitivity to the Parameters Characterizing the Stress Heterogeneities

[32] It is clear from section 4 that there are three basic parameters controlling results in the case of spatially heterogeneous initial shear stress: the amplitude of fluctuations ($B$), the random seed (both influencing the RMS of the imposed stress field) and the reference value of the strength parameter ($S^{(ref)}$). We performed many additional simulations of heterogeneous ruptures, and we can summarize conclusions as follows. In most cases (for large values of $B$ and $S^{(ref)}$) the rupture either does not propagate over more than a small portion of the fault or does not have supershear patches. On the contrary, when rupture has sufficiently large supershear regions, as in model C discussed above, Mach pulses are generated. When the initial shear stress distribution guarantees the occurrence of sufficiently large fault patches where rupture velocity is supershear, changes in the reference value of the strength parameter simply shift the synthetic seismograms in time, but do not obscure the presence of $M_S$ wavefront. This makes sense, since when we change $S^{(ref)}$ from one simulation to another we are not also changing the stress drop, which is probably what is most responsible for determining the amplitude of the velocity pulses. If one makes small changes in $S^{(ref)}$ while holding stress drop fixed, then the amplitude of the seismograms is approximately preserved. Of course, large changes in $S^{(ref)}$ will ultimately change the entire rupture process and thus the seismograms.

## 7. Spectra of Ground Velocities

[33] In this section we address two questions. First, what is the enrichment in frequency content (qualitatively discussed in section 5) in the heterogeneous supershear model (C) relative to its homogeneous counterpart (A)? Second, what is the relation between the Hurst exponent of the heterogeneities at large $k$ and the asymptotic behavior of the ground velocity spectrum?

[34] To investigate this we calculate Fourier amplitude spectra (FAS) of the components of ground velocity ($V_k$). To cause all FAS for all synthetic seismograms of all models to be calculated for the same set of frequencies (so that all spectra could be compared and ratios taken) we removed the first 5 s of all seismograms, which does not contain any meaningful signal at the receivers under consideration. Then we applied a half-cosine taper to the seismograms from 25 to 30 s (for models A and C) and from 40 s to 45 s (for model B). Beyond the end of the tapered region, all seismograms were extended by adding zeros to the end such that all of the seismograms have the same total length. Due to numerical dispersion, the calculated spectra are only valid up to approximately 7–8 Hz. The frequency increment in the FAS is about 0.01 Hz.

[35] The obtained FAS of $\mathbf{V}$ for models A, B and C, for the same free surface receiver considered in Figure 10, are reported in Figure 12. It is clear that the near-field contribution (static offset) at this receiver elevates the FAS at low frequency in the strike-parallel component of all models; the near-field contribution is even more significant at stations closer to the fault. Even at the farthest receiver we do not observe the $\omega^1$ behavior of the Brune spectrum [*Brune*, 1970] at low frequencies in the strike-parallel component as a consequence of the mixture of near-field and far-field terms. On the contrary, in the high frequency band (1–8 Hz, the range of primary interest of structural engineers, since the resonant frequencies of many structures lie in this band) the FAS of $\mathbf{V}$ for subshear homogeneous rupture (model B) decays asymptotically as roughly $\omega^{-1}$ (component 2) and as roughly $\omega^{-1.7}$ (components 1 and 3).

[36] The spectra of $\mathbf{V}$ pertaining to the supershear ruptures (models A and C) are not completely flat, as found in heterogeneous kinematic supershear models of BS08 (see their Figure 2), but they exhibit a decay that is less than that of subshear model B (they vary roughly as $\omega^{-0.7}$). The ratio of the FAS for models A and B (Figure 12d) shows that the amplification factor, within the frequency band 1–8 Hz, is roughly equal to $\omega^1$ (for components 1 and 3). We have verified that this is true also for other free surface receivers, provided that they are not too close to the fault (i.e., distances from the fault trace less than about 10 km) so that their spectra are not too strongly affected by the static offset (near-field term).

[37] Models A and C have very similar FAS, even at high frequencies, where the signal is dominated by the Mach pulses. Based on the ratio of their FAS (Figure 12e), there appears to be only a slight reduction in spectral content arising from the heterogeneities in model C. In the frequency range where seismograms are valid the ratio of the two FAS exhibits a variation that is nearly two orders of magnitude smaller than the variation in the ratio of the FAS of the two homogeneous models A and B (Figure 12d). This indicates that the heterogeneities in model C are contributing little to the high frequency seismograms; the Mach pulse in both models dominates the high frequencies. This result, valid also for other free surface receivers, is in agreement with results obtained with a kinematic model by BS08: ground velocity spectrum of supershear pulses is quite unaffected by the stress/slip heterogeneity spectrum, since it is primarily controlled by the spectrum of the fault slip velocity. As a consequence of properties of the Fourier transform ($F\ [V_k] = i\omega F\ [U_k]$, $\mathbf{U}$ being the ground displacement vector), it follows that, at high frequencies, supershear rupture propagation produces a displacement spectrum falloff roughly proportional to $\omega^{-1.7}$. This results is reasonable; we know the slip velocity of a supershear rup-

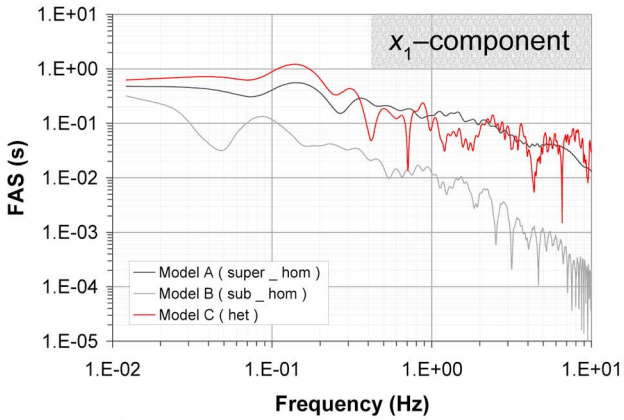


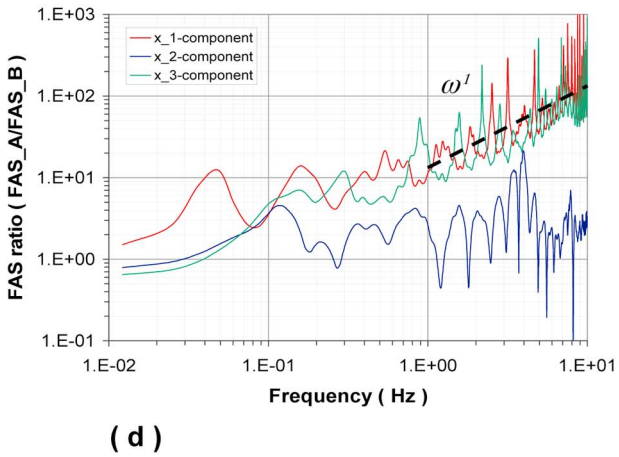


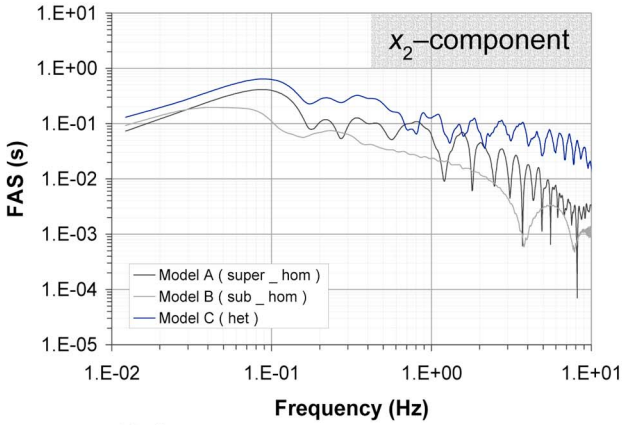


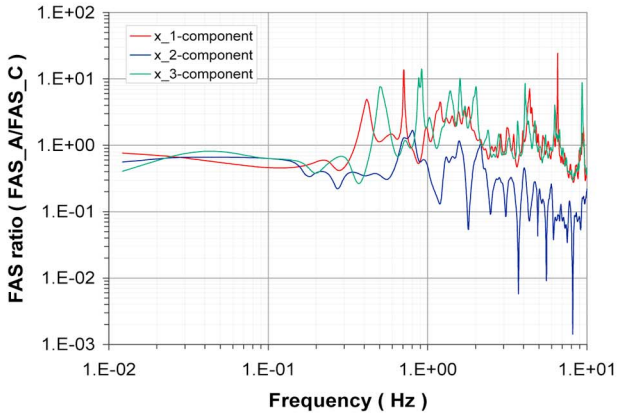


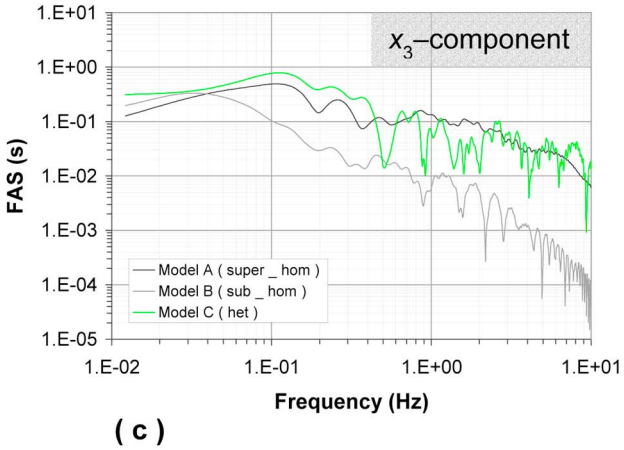


**Figure 12.** Spectral analysis of ground velocity at $(x_1, x_3) = (50,35)$ km (same as Figures 7 and 10) for models A, B, and C. Normalization of $V_k$ is the same as in Figures 5 and 6. Frequencies above 8 Hz are affected by numerical oscillations. (a–c) Comparison of FAS of three components of **V**. (d) Comparison between homogeneous models; the ratios $\mathrm{FAS}_{Vi}^{(A)}/\mathrm{FAS}_{Vi}^{(B)}$ indicate an amplification nearly equal to $\omega^1$ of supershear model with respect to the homogeneous subshear one. (e) Comparison between supershear models; the ratios $\mathrm{FAS}_{Vi}^{(A)}/\mathrm{FAS}_{Vi}^{(C)}$ do not show a specific trend, suggesting that the seismograms are essentially dominated by Mach pulses. Note the different scale range in Figures 12d and 12e.

ture has a singularity $r^{-\alpha}$, where $0 < \alpha \leq 0.5$ [*Andrews*, 1976]. If the particle velocity carried in the shear Mach waves is proportional to this (*Dunham and Archuleta* [2005] showed that this is exactly true for 2-D steady state ruptures and we showed it applies asymptotically in 3-D for sustained supershear propagation), then the Fourier spectrum of particle velocity should be the same as that of the slip velocity. Hence, the displacement spectrum should fall off as $\omega^{\alpha-2}$. For $\alpha = 0.3$ (a reasonable value for our rupture speeds), this gives $\omega^{-1.7}$, which is what we found.

## 8. Comparison With Empirical Data

[38] To determine whether observed high frequency ground motions are amplified by Mach pulses, we selected a set of stations at which Mach pulses are thought to have been experienced. To determine the Mach pulse stations in the 1979 Imperial Valley earthquake, we looked for minima in the *S* wave arrival time functions that we calculated for all stations using the rupture time model and seismic velocity structure of *Archuleta* [1984]. The stations having minima in their arrival time functions were Brawley, Calipatria, Coachella Canal, El Centro 1, 3, 4, 5, 6, 7, 8, 10, 11, El Centro County Services Building, El Centro Differential Array, Meloland, Niland, Parachute Test Site, Superstition Mountain Camera, and Westmorland. For the 1999 Kocaeli, Turkey, earthquake, the station Sakarya was identified by *Bouchon et al.* [2002], and we guessed from the geometry that station Goynuk was in a Mach zone. We also included station Pump Station 10 from the 2002 Denali Fault earthquake, which was identified by *Ellsworth et al.* [2004] and *Dunham and Archuleta* [2004] as having a Mach pulse. It is possible that there are other stations for other earthquakes (e.g., Duzce) having Mach pulses, but with the possible exception of Goynuk, all of the selected stations should have been in a Mach zone.

[39] If a subset of an earthquake's stations is illuminated by a Mach pulse, the high frequency motions at those stations should be greater than the motions at the earthquake's stations that are located outside the Mach zone (the region illuminated by a Mach pulse). In principle we should compare the high frequency Fourier amplitude spectra of stations inside and outside the Mach zone, but such a comparison is not straightforward because each station is at a different distance from the source, and the stations have varying soil conditions and depths to basement, all of which must be corrected for in the comparison. There is no good model of Fourier amplitude spectra which includes dependences on all these factors, but there are engineering models of absolute response spectral acceleration (SA), such as that of *Abrahamson and Silva* [2008], which includes all these factors. Consequently, we look for elevated motions within the Mach zone, compared to stations outside the zone, by looking at the intra-event residuals, with respect to the Abrahamson and Silva predicted median motions, of the Mach pulse stations for 5%-damped SA at oscillator periods 0.05, 0.75, 0.1, 0.15, 0.2, 0.3, and 0.4 s. A practical advantage of examining SA rather than Fourier spectra is that SA is the spectral quantity most commonly used by engineers, and thus examination of Mach pulse effects on SA would be the most relevant to engineering practice. We did not consider SA at very short periods (e.g., 0.01 s), where it is equivalent to peak ground acceleration, because the seismograms used by Abrahamson and Silva were low-pass-filtered differently from each other. The intra-event residual is the natural log of the observed SA, for the selected period, for each event, minus the log of the predicted SA minus the 'event term', which is the mean of the intra-event residuals over all stations for a selected period. Presumably, if the Mach pulse is amplifying the high frequency motions, the amplified stations will have a positive intra-event residual.

[40] Figure 13a shows that the short-period SA at Mach pulse stations is not systematically elevated above the Abrahamson and Silva prediction. In addition, because the mean intra-event residual over all stations for each earthquake is zero, Figure 13a implicitly shows that on the average the Mach pulse stations' ground motions are not elevated above the non-Mach pulse stations for each earthquake. The square and the diamond show that, in fact, Sakarya and Pump Station 10 are low compared to a ground motion prediction relation fitted through the other Kocaeli and Denali stations. Of course, the intra-event residuals are calculated with respect to a ground motion prediction relation fitted through the entire NGA data set, including the three earthquakes considered.

[41] We tried to find Mach pulse amplification in various subsets of Mach pulse stations, and it is only for Imperial Valley stations E05, E06, E07, E08, and EDA, the stations on the cross array closest to the fault, that we were able to find an elevated intra-event residual of about 0.2, corresponding to about a 20% increase in short period ground motions (Figure 13c). This increase might be true Mach pulse amplification, or it might be related to proximity to the slip maximum. Intra-event residuals at Meloland, also very close to the fault, were negative, indicating no Mach pulse amplification.

[42] Because the Imperial Valley earthquake is the most well recorded M 6.5 event in the data set, it might be that the fitted SA-prediction relationship already includes Mach pulse amplification for most stations except the nearest. However, if this is the case, it means that the predictive relations used by engineers for M 6.5 earthquakes already contain Mach pulse amplification, and possibly only a 20% additional modification is needed at high frequency.

[43] If it is true that there is no Mach pulse amplification to be seen at most Mach zone stations in Figure 13, where has it gone? A possibility for the Imperial Valley is that nonlinear soil response in the shallow alluvium has strongly attenuated the high frequencies. *Ellsworth et al.* [2004] have noted that strains at Pump Station 10 were probably in the nonlinear range. It might be that Mach pulses systematically cause their own extinction. Another possibility is that the degree of source heterogeneity in nature is even higher than in our simulations, completely disrupting the Mach pulse. It might be that a highly complicated rupture time function would lead to much more rapid geometrical spreading than the lossless spreading caused by a straight rupture front [*Bernard and Baumont*, 2005; *Dunham and Bhat*, 2008]. Equations (5) and (7) of *Bizzarri and Spudich* [2008] show how the spreading is related to the curvature of the arrival time function. Other possible explanations are (1) that crustal scattering of the *S* wave reduced the Mach pulse coherence, (2) Archuleta's rupture time model is inaccurate

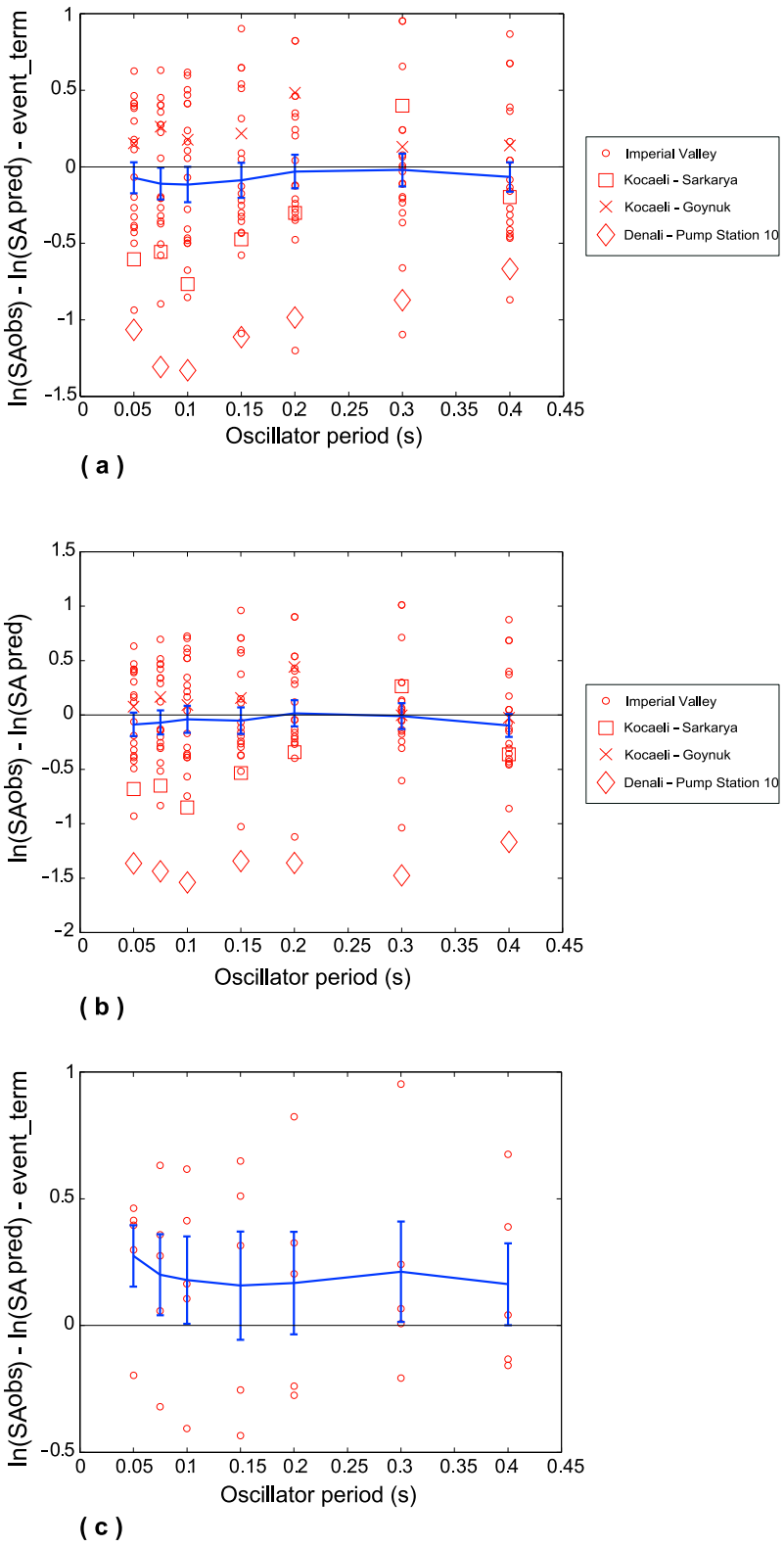


**Figure 13.** Comparison of 5%-damped spectral acceleration (SA), at oscillator periods of 0.05 s, 0.75 s, 0.1 s and 0.2 s, observed and predicted at stations thought to have experienced a Mach pulse in recent earthquakes. Predicted SA from *Abrahamson and Silva* [2008]. The heavy blue lines indicate the mean value of SA residual and its standard error at each period. (a) Intra-event residuals (log of the observed SA minus log of the predicted, minus the "event term"). (b) Total residuals (log of the observed SA minus log of the predicted) for the same stations and periods. (c) Intra-event residuals for Imperial Valley stations on the cross array closest to the fault (stations E05, E06, E07, E08, and EDA).

and some stations that we have identified as receiving Mach pulses did not in fact do so, or (3) there was no supershear rupture propagation in the earthquake.

[44] The picture is similar when we look at total residuals to the *Abrahamson and Silv*a [2008] relation in Figure 13b, i.e., the difference of the natural log of the observed SA, for the selected period and the log of the predicted SA from the Abrahamson and Silva's relation, with no removal of the "event term." This shows that considering all Mach pulse stations, the observed motions agree on the average with the motions predicted by *Abrahamson and Silva* [2008].

## 9. Conclusions

[45] The basic objective of the present paper is to investigate whether or not shear and Rayleigh Mach fronts from supershear ruptures remain coherent when rupture process is irregular (i.e., more complicated with respect to a homogeneous rupture with planar front propagating at constant speed, as in DB08). To address this, we have numerically solved the elastodynamic equation, neglecting body forces for a single, planar, vertical, strike slip fault, embedded in an homogeneous, elastic half-space. The fault is governed by the linear slip-weakening friction law, either with homogeneous and heterogeneous initial shear stress. The synthetic earthquake ruptures are fully dynamic (in that inertia is always accounted for), spontaneous (in that rupture velocity is determined as a part of the solution of the problem) and truly 3-D (in that both components of the solutions are nonzero and both depend on the two on-fault coordinates; the rupture front is curved and rake rotation is permitted).

[46] The homogeneous stress cases presented in this study (models A and B; see section 3) clearly confirm in 3-D spontaneous earthquake models the conclusions of DB08, based on ruptures forced to propagate at constant speed with straight rupture fronts. Our numerical models indicate that the main features described by DB08 regarding the wavefield of supershear and subshear ruptures are not altered by rupture front curvature alone: supershear ruptures generate both shear and Rayleigh Mach waves and that these Mach waves transmit significant stress perturbations and ground motion much farther from the fault than in a subshear earthquake. However, generation of the Rayleigh Mach wave may be diminished in rupture models having little near-surface slip or low stress drop near the surface.

[47] Moreover, we can conclude that the introduction of heterogeneities in the initial shear stress (model C; see sections 4 and 5) does not obscure the generation of Mach waves in the case of a rupture that propagates, on average, with supershear speed, but has some patches that remain subshear.

[48] We have also seen that heterogeneous propagation reduces the peak ground velocity and decreases Mach front coherence (see Figure 11b). The loss of coherence is due to two reasons. First, the variability in rupture velocity (see Figure 8d), which locally fluctuates above and below the shear wave speed, causes the $S$ wave isochrone velocity to be singular at many different fault points (see Figure 11a), each of which emits a shear Mach pulse. Second, the fault slip velocity time histories are spatially less correlated in heterogeneous models than in homogeneous ones (see Figures 11a, 11b, and 11c).

[49] Moreover, calculations of the Fourier amplitude spectra (FAS) of ground velocity in our models show that the ground motion at stations experiencing Mach pulses is elevated, at high frequencies, by a factor of roughly $\omega$ above that recorded at similarly located stations in a homogeneous rupture model without Mach pulses (see Figure 12d). In other words, the ground motion of a supershear rupture is richer in high frequencies with respect to that from a homogeneous subshear rupture in these numerical models. We also found that, when a Mach pulse is present, its high frequency content overwhelms the high frequencies introduced by stress/slip heterogeneity (see Figure 12e), corroborating the kinematic results of BS08. Given these theoretical results, it is surprising that Mach pulses are not very clear in real earthquake seismograms. In fact, by considering data from stations that presumably experienced Mach pulses (during the 1979 Imperial Valley, 1999 Kocaeli, and 2002 Denali Fault earthquakes), we find no elevation of 5%-damped response spectral accelerations (SA) in the period band 0.05–0.4 s compared to SA observed at non-Mach pulse stations in the same earthquakes. It is only for a small subset of Imperial Valley stations that we find a possible Mach pulse amplification of 20%. This general lack of elevated SA suggests that either Mach pulses in real earthquakes are even more incoherent that in our numerical experiments or Mach pulses are vulnerable to attenuation through nonlinear soil response.

[50] Our results also indicate that both uniform supershear rupture and mixed subshear and supershear rupture in model having a $k^{-1}$ initial shear stress heterogeneity (corresponding to a $k^{-2}$ spectral decay rate of slip in the Fourier domain) cause an $\omega^{-1.7}$ high frequency falloff in the FAS of ground displacement.

[51] Finally, we want to remark that due to intrinsic limitations of the employed numerical method, in order to have a proper resolution of the cohesive zone and reasonable computational times, we were not able to consider a small characteristic slip-weakening distance compared to the size of heterogeneities of the initial shear stress. With the relatively large $d_0$ that we adopted in this work, ruptures are not very responsive the imposed heterogeneities and therefore there is not a dramatic alteration in the coherence of the Mach front. We believe that further studies with better numerical methods and higher resolution will be essential to definitively resolving the issue of the coherence of Mach fronts, which may be important in assessing hazard from supershear ruptures.

[52] **Acknowledgments.** We thank Harsha Bhat for early discussions about the main motivations of this paper and André Herrero for some comments on $\omega^{-2}$ model. D. J. Andrews and D. M. Boore are kindly acknowledged for their preliminary review of the paper. We are also grateful to Tom Parsons, to the Associate Editor, and to S. M. Day for their stimulating remarks.

## References

Aagaard, B. T., and T. H. Heaton (2004), Near-source ground motions from simulations of sustained intersonic and supersonic fault ruptures, *Bull. Seismol. Soc. Am.*, *94*(6), 2064–2078, doi:10.1785/0120030249.

Abrahamson, N., and W. Silva (2008), Summary of the Abrahamson & Silva NGA ground-motion relations, *Earthquake Spectra*, *24*, 67–97, doi:10.1193/1.2924360.

Andrews, D. J. (1976), Rupture velocity of plane strain shear cracks, *J. Geophys. Res.*, *81*, 5679–5687, doi:10.1029/JB081i032p05679.

Andrews, D. J. (1980), Fault impedance and earthquake energy in the Fourier transform domain, *Bull. Seismol. Soc. Am.*, *70*(5), 1683–1698.

Archuleta, R. J. (1984), A faulting model for the 1979 Imperial Valley earthquake, *J. Geophys. Res.*, *89*, 4559–4585, doi:10.1029/JB089iB06p04559.

Berge-Thierry, C., P. Bernard, and A. Herrero (2001), Simulating strong ground motion with the '*k*-2' kinematic source model: An application to the seismic hazard in the Erzincan basin, Turkey, *J. Seismol.*, *5*, 85–101, doi:10.1023/A:1009829129344.

Bernard, P., and D. Baumont (2005), Shear Mach wave characterization for kinematic fault rupture models with constant super-shear rupture velocity, *Geophys. J. Int.*, *162*, 431–447, doi:10.1111/j.1365-246X.2005.02611.x.

Bernard, P., and R. Madariaga (1984), A new asymptotic method for the modeling of near field accelerograms, *Bull. Seismol. Soc. Am.*, *74*, 539–558.

Bhat, H. S., R. Dmowska, G. C. P. King, Y. Klinger, and J. R. Rice (2007), Off-fault damage patterns due to supershear ruptures with application to the 2001 Mw 8.1 Kokoxili (Kunlun) Tibet earthquake, *J. Geophys. Res.*, *112*, B06301, doi:10.1029/2006JB004425.

Bizzarri, A. (2009), What does control earthquake ruptures and dynamic faulting? A review of different competing mechanisms, *Pure Appl. Geophys.*, *166*(5–7), 741–776, doi:10.1007/s00024-009-0494-1.

Bizzarri, A. (2010), How to promote earthquake ruptures: Different nucleation strategies in a dynamic model with slip-weakening friction, *Bull. Seismol. Soc. Am.*, *100*(3), 923–940, doi:10.1785/0120090179.

Bizzarri, A., and M. Cocco (2005), 3D dynamic simulations of spontaneous rupture propagation governed by different constitutive laws with rake rotation allowed, *Ann. Geophys.*, *48*(2), 279–299.

Bizzarri, A., and M. Cocco (2006), Comment on "Earthquake cycles and physical modeling of the process leading up to a large earthquake," *Earth Planets Space*, *58*, 1525–1528.

Bizzarri, A., and P. Spudich (2008), Effects of supershear rupture speed on the high-frequency content of S waves investigated using spontaneous dynamic rupture models and isochrone theory, *J. Geophys. Res.*, *113*, B05304, doi:10.1029/2007JB005146.

Bizzarri, A., M. Cocco, D. J. Andrews, and E. Boschi (2001), Solving the dynamic rupture problem with different numerical approaches and constitutive laws, *Geophys. J. Int.*, *144*, 656–678, doi:10.1046/j.1365-246x.2001.01363.x.

Bouchon, M., and M. Vallée (2003), Observation of long supershear rupture during the magnitude 8.1 Kunlunshan earthquake, *Science*, *301*, 824–826, doi:10.1126/science.1086832.

Bouchon, M., M. N. Toksöz, H. Karabulut, M.-P. Bouin, M. Dietrich, M. Aktar, and M. Edie (2000), Seismic imaging of the 1999 Izmit (Turkey) rupture inferred from the near-fault recordings, *Geophys. Res. Lett.*, *27*, 3013–3016, doi:10.1029/2000GL011761.

Bouchon, M., M.-P. Bouin, H. Karabulut, M. N. Toksöz, M. Dietrich, and A. J. Rosakis (2001), How fast is rupture during an earthquake? New insights from the 1999 Turkey earthquakes, *Geophys. Res. Lett.*, *28*, 2723–2726, doi:10.1029/2001GL013112.

Bouchon, M., M. N. Toksöz, H. Karabulut, M.-P. Bouin, M. Dietrich, M. Aktar, and M. Edie (2002), Space and time evolution of rupture and faulting during the 1999 Izmit (Turkey)earthquake, *Bull. Seismol. Soc. Am.*, *92*(1), 256–266, doi:10.1785/0120000845.

Broberg, K. B. (1994), Intersonic bilateral slip, *Geophys. J. Int.*, *119*, 706–714, doi:10.1111/j.1365-246X.1994.tb04010.x.

Broberg, K. B. (1995), Intersonic mode II crack expansion, *Arch. Mech.*, *47*, 859–871.

Brune, J. (1970), Tectonic stress and the spectra of seismic shear waves from earthquakes, *J. Geophys. Res.*, *75*, 4997–5009, doi:10.1029/JB075i026p04997.

Burridge, R. (1973), Admissible speeds for plane-strain self-similar shear cracks with friction but lacking cohesion, *Geophys. J. R. Astron. Soc.*, *35*, 439–455.

Campbell, K. C., and Y. Bozorgnia (2008), Campbell-Bozorgnia NGA horizontal ground motion model for PGA, PGV, PGD, and 5% damped linear elastic response spectra, *Earthquake Spectra*, *24*, 139–171, doi:10.1193/1.2857546.

Dalguer, L. A., and S. M. Day (2007), Staggered-grid split-node method for spontaneous rupture simulation, *J. Geophys. Res.*, *112*, B02302, doi:10.1029/2006JB004467.

Das, S. (1981), Three-dimensional spontaneous rupture propagation and implications for the earthquake source mechanism, *Geophys. J. R. Astron. Soc.*, *67*, 375–393.

Das, S., and K. Aki (1977), A numerical study of two-dimensional spontaneous rupture propagation, *Geophys. J. R. Astron. Soc.*, *50*, 643–668.

Day, S. M. (1982), Three-dimensional simulation of spontaneous rupture: The effect of nonuniform prestress, *Bull. Seismol. Soc. Am.*, *72*, 1881–1902.

Dunham, E. M. (2007), Conditions governing the occurrence of supershear ruptures under slip-weakening friction, *J. Geophys. Res.*, *112*, B07302, doi:10.1029/2006JB004717.

Dunham, E. M., and J. R. Archuleta (2004), Evidence for a super-shear transient during the 2002 Denali fault earthquake, *Bull. Seismol. Soc. Am.*, *94*(6B), S256–S268, doi:10.1785/0120040616.

Dunham, E. M., and J. R. Archuleta (2005), Near-source ground motion from steady state dynamic rupture pulses, *Geophys. Res. Lett.*, *32*, L03302, doi:10.1029/2004GL021793.

Dunham, E. M., and H. S. Bhat (2008), Attenuation of radiated ground motion and stresses from three-dimensional supershear ruptures, *J. Geophys. Res.*, *113*, B08319, doi:10.1029/2007JB005182.

Dunham, E. M., P. Favreau, and J. M. Carlson (2003), A supershear transition mechanism for cracks, *Science*, *299*, 1557–1559, doi:10.1126/science.1080650.

Ellsworth, W. L., M. Celebi, J. R. Evans, E. G. Jensen, M. C. Metz, D. J. Nyman, J. W. Roddick, P. Spudich, and C. D. Stephens (2004), Near-field ground motions of the *M* 7.9 November 3, 2002, Denali fault, Alaska, earthquake recorded at pump station 10, *Earthquake Spectra*, *20*, 597–615, doi:10.1193/1.1778172.

Eshelby, J. D. (1949), Uniformly moving dislocations, *Proc. Phys. Soc. London, Sect. A*, *62*, 307–314, doi:10.1088/0370-1298/62/5/307.

Favreau, P., M. Campillo, and I. R. Ionescu (2002), Initiation of shear instability in three-dimensional elastodynamics, *J. Geophys. Res.*, *107*(B7), 2147, doi:10.1029/2001JB000448.

Frankel, A., and R. W. Clayton (1986), Finite difference simulations of seismic scattering: Implications for the propagation of short-period seismic waves in the crust and models of crustal heterogeneity, *J. Geophys. Res.*, *91*, 6465–6489, doi:10.1029/JB091iB06p06465.

Freund, L. B. (1979), The mechanics of dynamic shear crack propagation, *J. Geophys. Res.*, *84*, 2199–2209, doi:10.1029/JB084iB05p02199.

Fukuyama, E., and K. B. Olsen (2002), A condition for supershear rupture propagation in a heterogeneous stress field, *Pure Appl. Geophys.*, *159*, 2047–2056, doi:10.1007/s00024-002-8722-y.

Harris, R. A., et al. (2009), The SCEC/USGS dynamic earthquake rupture code verification exercise, *Seismol. Res. Lett.*, *80*(1), 119–126, doi:10.1785/gssrl.80.1.119.

Heaton, T. H. (1990), Evidence for and implications of self-healing pulses of slip in earthquake rupture, *Phys. Earth Planet. Inter.*, *64*, 1–20, doi:10.1016/0031-9201(90)90002-F.

Herrero, A., and P. Bernard (1994), A kinematic self-similar rupture process for earthquakes, *Bull. Seismol. Soc. Am.*, *84*, 1216–1228.

Ida, Y. (1972), Cohesive force across the tip of a longitudinal-shear crack and Griffith's specific surface energy, *J. Geophys. Res.*, *77*, 3796–3805, doi:10.1029/JB077i020p03796.

Madariaga, R. (1983), High frequency radiation from dynamics earthquake fault models, *Ann. Geophys.*, *1*(17), 17–23.

Mai, P. M., and G. C. Beroza (2002), A spatial random field model to characterize complexity in earthquake slip, *J. Geophys. Res.*, *107*(B11), 2308, doi:10.1029/2001JB000588.

Needleman, A. (1999), An analysis of intersonic crack growth under shear loading, *J. Appl. Mech.*, *66*(4), 847–857, doi:10.1115/1.2791788.

Okubo, P. G. (1989), Dynamic rupture modeling with laboratory-derived constitutive relations, *J. Geophys. Res.*, *94*, 12,321–12,335, doi:10.1029/JB094iB09p12321.

Robinson, D. P., C. Brough, and S. Das (2006), The $M_w$ 7.8, 2001 Kunlunshan earthquake: Extreme rupture speed variability and effect of fault geometry, *J. Geophys. Res.*, *111*, B08303, doi:10.1029/2005JB004137.

Rosakis, A. J., O. Samudrala, and D. Coker (1999), Cracks faster than the shear-wave speed, *Science*, *284*, 1337–1340, doi:10.1126/science.284.5418.1337.

Samudrala, O., Y. Huang, and A. J. Rosakis (2002), Subsonic and intersonic shear rupture of weak planes with a velocity weakening cohesive zone, *J. Geophys. Res.*, *107*(B8), 2170, doi:10.1029/2001JB000460.

Shakal, A., V. Graizer, M. Huang, R. Borcherdt, H. Haddadi, K.-w. Lin, C. Stephens, and P. Roffers (2005), Preliminary analysis of strong-motion recordings from the 28 September 2004 Parkfield, California earthquake, *Seismol. Res. Lett.*, *76*(1), 27–39, doi:10.1785/gssrl.76.1.27.

Song, S. G., G. C. Beroza, and P. Segall (2008), A unified source model for the 1906 San Francisco earthquake, *Bull. Seismol. Soc. Am.*, *98*(2), 823–831, doi:10.1785/0120060402.

Spudich, P. (1992), On the inference of absolute stress levels from seismic radiation, *Tectonophysics*, *211*, 99–106, doi:10.1016/0040-1951(92)90053-9.

Spudich, P., and E. Cranswick (1984), Direct observation of rupture propagation during the 1979 Imperial Valley earthquake using a short baseline accelerometer array, *Bull. Seismol. Soc. Am.*, *74*, 2083–2114.

Spudich, P., and L. N. Frazer (1984), Use of ray theory to calculate high-frequency radiation from earthquake sources having spatially variable rupture velocity and stress drop, *Bull. Seismol. Soc. Am.*, *74*, 2061–2082.

Vallée, M., M. Landès, N. M. Shapiro, and Y. Klinger (2008), The 14 November 2001 Kokoxili (Tibet) earthquake: High-frequency seismic radiation originating from the transitions between sub-Rayleigh and supershear rupture velocity regimes, *J. Geophys. Res.*, *113*, B07305, doi:10.1029/2007JB005520.

Walker, K. T., and P. M. Shearer (2009), Illuminating the near-sonic rupture velocities of the intracontinental Kokoxili $M_w$ 7.8 and Denali fault $M_w$ 7.9 strike-slip earthquakes with global *P* wave back projection imaging, *J. Geophys. Res.*, *114*, B02304, doi:10.1029/2008JB005738.

Wu, F. T., K. C. Thomson, and H. Kuenzler (1972), Stick-slip propagation velocity and seismic source mechanism, *Bull. Seismol. Soc. Am.*, *62*, 1621–1628.

Xia, K., A. J. Rosakis, and H. Kanamori (2004), Laboratory experiments: The sub-Rayleigh-to-supershear rupture transition, *Science*, *303*, 1859–1861, doi:10.1126/science.1094022.

A. Bizzarri, Istituto Nazionale di Geofisica e Vulcanologia, Sezione di Bologna, Via Donato Creti, 12, I-40128 Bologna, Italy. (bizzarri@bo.ingv.it)

E. M. Dunham, Geophysics Department, Stanford University, Mitchell Bldg., Rm. 325, 397 Panama Mall, Stanford, CA 94305-2215, USA.

P. Spudich, U.S. Geological Survey, 345 Middlefield Rd., MS977, Menlo Park, CA 94025, USA.